

## Generalized inhomogeneity-resilient relaxation along a fictitious field (girRAFF) for improved robustness in rotating frame relaxometry at 3T

Coletti, Chiara; Naaktgeboren, Roeland; Tourais, Joao; Van De Steeg-Henzen, Christal; Weingärtner, Sebastian

**DOI**

[10.1002/mrm.30219](https://doi.org/10.1002/mrm.30219)

**Publication date**

2024

**Document Version**

Final published version

**Published in**

Magnetic Resonance in Medicine

**Citation (APA)**

Coletti, C., Naaktgeboren, R., Tourais, J., Van De Steeg-Henzen, C., & Weingärtner, S. (2024). Generalized inhomogeneity-resilient relaxation along a fictitious field (girRAFF) for improved robustness in rotating frame relaxometry at 3T. *Magnetic Resonance in Medicine*, 92(6), 2373-2391. <https://doi.org/10.1002/mrm.30219>

**Important note**

To cite this publication, please use the final published version (if applicable).  
Please check the document version above.

**Copyright**

Other than for strictly personal use, it is not permitted to download, forward or distribute the text or part of it, without the consent of the author(s) and/or copyright holder(s), unless the work is under an open content license such as Creative Commons.

**Takedown policy**

Please contact us and provide details if you believe this document breaches copyrights.  
We will remove access to the work immediately and investigate your claim.

# Generalized inhomogeneity-resilient relaxation along a fictitious field (girRAFF) for improved robustness in rotating frame relaxometry at 3T

Chiara Coletti<sup>1</sup>  | Roeland Naaktgeboren<sup>1</sup> | Joao Tourais<sup>1</sup>  |  
Christal Van De Steeg-Henzen<sup>2</sup> | Sebastian Weingärtner<sup>1,2</sup> 

<sup>1</sup>Department of Imaging Physics, Delft University of Technology, Delft, The Netherlands

<sup>2</sup>HollandPTC, Delft, The Netherlands

## Correspondence

Sebastian Weingärtner, Department of Imaging Physics, Delft University of Technology, Lorentzweg 1, 2628 CJ, Delft, The Netherlands.

Email: [S.Weingartner@tudelft.nl](mailto:S.Weingartner@tudelft.nl)

## Funding information

ZonMw, Grant/Award Number: 04510011910073; Nederlandse Organisatie voor Wetenschappelijk Onderzoek, Grant/Award Number: STU.019.024; TU Delft - Erasmus MC Convergence Impulse Award; European Research Council, Grant/Award Number: 101078711; 4TU Precision Medicine program supported by High Tech for a Sustainable Future

## Abstract

**Purpose:** To optimize Relaxation along a Fictitious Field (RAFF) pulses for rotating frame relaxometry with improved robustness in the presence of  $B_0$  and  $B_1^+$  field inhomogeneities.

**Methods:** The resilience of RAFF pulses against  $B_0$  and  $B_1^+$  inhomogeneities was studied using Bloch simulations. A parameterized extension of the RAFF formulation was introduced and used to derive a generalized inhomogeneity-resilient RAFF (girRAFF) pulse. RAFF and girRAFF preparation efficiency, defined as the ratio of the longitudinal magnetization before and after the preparation ( $M_z(T_p)/M_0$ ), were simulated and validated in phantom experiments.  $T_{\text{RAFF}}$  and  $T_{\text{girRAFF}}$  parametric maps were acquired at 3T in phantom, the calf muscle, and the knee cartilage of healthy subjects. The relaxation time maps were analyzed for resilience against artificially induced field inhomogeneities and assessed in terms of in vivo reproducibility.

**Results:** Optimized girRAFF preparations yielded improved preparation efficiency (0.95/0.91 simulations/phantom) with respect to RAFF (0.36/0.67 simulations/phantom).  $T_{\text{girRAFF}}$  preparations showed in phantom/calf 6.0/4.8 times higher resilience to  $B_0$  inhomogeneities than RAFF, and a 4.7/5.3 improved resilience to  $B_1^+$  inhomogeneities. In the knee cartilage,  $T_{\text{girRAFF}}$  ( $53 \pm 14$  ms) was higher than  $T_{\text{RAFF}}$  ( $42 \pm 11$  ms). Moreover, girRAFF preparations yielded 7.6/4.9 times improved reproducibility across  $B_0/B_1^+$  inhomogeneity conditions, 1.9 times better reproducibility across subjects and 1.2 times across slices compared with RAFF. Dixon-based fat suppression led to a further 15-fold improvement in the robustness of girRAFF to inhomogeneities.

**Conclusions:** RAFF pulses display residual sensitivity to off-resonance and pronounced sensitivity to  $B_1^+$  inhomogeneities. Optimized girRAFF pulses provide increased robustness and may be an appealing alternative for applications where resilience against field inhomogeneities is required.

## KEYWORDS

$B_0/B_1^+$  inhomogeneities, RAFF, relaxation mapping, RF pulse design, rotating-frame of reference

Chiara Coletti and Roeland Naaktgeboren contributed equally to this work.

This is an open access article under the terms of the [Creative Commons Attribution](https://creativecommons.org/licenses/by/4.0/) License, which permits use, distribution and reproduction in any medium, provided the original work is properly cited.

© 2024 The Author(s). *Magnetic Resonance in Medicine* published by Wiley Periodicals LLC on behalf of International Society for Magnetic Resonance in Medicine.

## 1 | INTRODUCTION

Quantitative MRI is a rapidly growing research area as it enables intra-subject comparable tissue characterization.<sup>1-4</sup> Conventional MRI relaxation times,  $T_1$  and  $T_2$ , are most commonly used.<sup>5</sup> Rotating frame relaxation times, such as  $T_{1\rho}$ , offer complementary contrast information to  $T_1$  and  $T_2$ , with increased sensitivity to slow molecular motion and chemical exchange.<sup>6-11</sup>

$T_{1\rho}$  describes the longitudinal relaxation in a rotating frame of reference (RFR), commonly measured during radiofrequency irradiation through continuous-wave spin-lock (SL) pulses. However, these SL pulses require a high specific absorption rate (SAR) burden and are highly susceptible to field inhomogeneities.<sup>12,13</sup> This hinders their applicability in clinical practice, especially at high field strengths ( $\geq 3T$ ). Improved resilience against field inhomogeneities can be achieved with adiabatic  $T_{1\rho}$ .<sup>14-17</sup> However, the pulses in adiabatic  $T_{1\rho}$  commonly exhibit a nonconstant effective and fictitious field, leading to differences in sensitivity compared with conventional SL pulses.<sup>18,19</sup>

To surmount the SAR constraints of continuous-wave SL while still exhibiting favorable sensitivity to slow molecular motion, Relaxation Along a Fictitious Field (RAFF) was proposed.<sup>20</sup> RAFF pulses are amplitude- and frequency-modulated (AM and FM) pulses that operate in a sub-adiabatic regime.<sup>20</sup> During the RAFF pulse, the behavior of the magnetic field can be described in a double-RFR, where the effective field in the second RFR acts as a spin-locking field.<sup>14</sup> Thus, RAFF generalizes spin-locking for higher-order rotating frames, while  $T_{1\rho}$  operates in the first RFR. This allows for larger spin-locking field amplitude by increasing only the fictitious field component while maintaining the effective field amplitude within SAR limits.<sup>21</sup>  $T_{\text{RAFF}}$  times have shown promise for tissue characterization in a number of preclinical and clinical studies across various field strengths.<sup>11,22-28</sup> While conventional RAFF pulses have shown moderate resilience against  $B_0$  inhomogeneities, they exhibit high sensitivity to  $B_1^+$  variations.<sup>20,29</sup> Resilience against off-resonances can be improved by using RAFF in higher-order rotating frames (RAFFn),<sup>29</sup> but sensitivity to  $B_1^+$  inhomogeneity remains a barrier to widespread clinical use.

In this study, we characterize the performances of RAFF pulses in the presence of  $B_0$  and  $B_1^+$  variations at 3T. Next, we introduce a parametric formulation of the conventional RAFF pulse to enable tailored off-resonance and  $B_1^+$  resilience. Based on this we propose a Generalized inhomogeneity-resilient RAFF (girRAFF) pulse to improve both  $B_0$  and  $B_1^+$  resilience. Data acquired in

phantom and in the calf muscle of healthy subjects are used to compare the performances of conventional RAFF and optimized girRAFF preparations in the presence of field inhomogeneities. Quantitative mapping quality and robustness to system imperfections are compared for RAFF and girRAFF pulses in the knee cartilage. Finally, the reproducibility of quantitative mapping using RAFF and girRAFF is assessed in the calf and the articular cartilage of healthy subjects.

## 2 | METHODS

### 2.1 | girRAFF pulse design

RAFF pulses are amplitude- and frequency-modulated radiofrequency pulses designed to achieve constant and equal effective ( $B_{\text{eff}}(t)$ ) and fictitious field ( $F(t)$ ) in the second RFR<sup>20</sup>:

$$F(t) \triangleq \gamma^{-1} \frac{d\alpha(t)}{dt} = B_{\text{eff}}(t). \quad (1)$$

Here,  $\gamma$  is the gyromagnetic ratio and  $\alpha(t)$  indicates the tilt angle of the effective field  $B_{\text{eff}}(t)$  relative to the  $z'$ -axis in the first RFR. The first RFR is defined by convention as rotating with the time-variant SL pulse frequency  $\omega_1(t)$  around the  $z$ -axis of the laboratory frame of reference ( $z = z'$ ). The second RFR, instead, is defined as rotating around  $y'$  with  $B_{\text{eff}}(t)$ , such that  $y' = y''$  and  $B_{\text{eff}}(t)$  is locked on  $z''$ . The fictitious field  $F(t)$  in the second RFR originates from the rotation of  $B_{\text{eff}}(t)$  around the  $y'$ -axis. During RAFF pulses the magnetization is effectively locked along the effective field in the second RFR:

$$E(t) = \sqrt{B_{\text{eff}}^2(t) + (\gamma^{-1} d\alpha(t)/dt)^2}. \quad (2)$$

The RAFF AM and FM functions are given by:

$$\omega_1(t) = \omega_{\text{max}} \sin(\omega_{\text{max}} t); \quad (3)$$

$$\Delta\omega_1(t) = \omega_{\text{max}} \cos(\omega_{\text{max}} t), \quad (4)$$

with  $\omega_{\text{max}}$  as the maximum pulse frequency. The pulse duration is set to  $T_{p,\text{RAFF}} = \frac{4\pi}{\sqrt{2}\omega_{\text{max}}}$  to effectively achieve 90° of rotation in both the first and second RFR.

The conditions in Equation (1) can be relaxed to allow for constant but nonequal effective and fictitious field strength, similar to the approach used by Liimatainen et al. for RAFF dispersion measurements.<sup>21</sup> To this end, we propose to generalize Equations (3) and (4) with 3 degrees of freedom,  $\theta, \nu, \rho$ . The proposed Generalized Inhomogeneities Resilient RAFF (girRAFF) amplitude and frequency modulation functions can then be written as:

$$\omega_1(t) = \omega_{\max} \sin\left(\frac{\omega_{\max}}{\nu} t - \theta\right), \quad (5)$$

$$\Delta\omega_1(t) = \omega_{\max} \cos\left(\frac{\omega_{\max}}{\nu} t - \theta\right), \quad (6)$$

with  $T_{p,\text{girRAFF}} = \rho T_{p,\text{RAFF}}$ .

Here  $\nu$  determines the ratio of the fictitious and effective field strength, with  $\nu = 1$  in conventional RAFF (Equation 1), while large  $\nu$  values satisfy the adiabatic condition.  $\theta$  denotes the starting angle of  $B_{\text{eff}}(t)$  with respect to the  $z'$ -axis (for RAFF:  $\theta = 0$ ). Finally,  $\rho$  is the scaling coefficient determining the girRAFF pulse duration relative to conventional RAFF, where  $\rho = 1$  yields the original RAFF pulse duration.

Figures S1–S3 illustrate the effects of the design parameters  $\theta$ ,  $\nu$ , and  $\rho$  on the pulse amplitude and frequency modulation functions. Examples of effective field  $B_{\text{eff}}(t)$  and magnetization  $M$  trajectories for representative values of  $\theta$ ,  $\nu$ , and  $\rho$  are also depicted in the first RFR in Figures S1–S3. As proposed for RAFF, the complete preparation modules are formed by concatenating four (gir)RAFF segments using a P-packet scheme, as described by Liimatainen et al.<sup>20</sup>

## 2.2 | Simulations

Bloch simulations were implemented in Python 3.6<sup>30</sup> to study the performance of RAFF and girRAFF pulses in the presence of  $B_0$  and  $B_1^+$  inhomogeneities, neglecting relaxation effects. The preparation efficiency of a pulse module was defined as the ratio between the longitudinal magnetization before and after the module ( $M_z(T_p)/M_0$ ). Here, a preparation efficiency value of +1, indicating fully balanced (gir)RAFF preparation schemes, with no  $B_0/B_1^+$  inhomogeneity-related distortions, was considered optimal. Additionally, the magnetization trajectory length throughout (gir)RAFF irradiation was measured as a metric to ensure sufficient excursion of the magnetization and, consequently, spin-locking efficacy. The trajectory length was computed as the cumulative sum of the discretized angular distances covered by the magnetization vector on the Bloch sphere during simulations. All simulations were limited by the peak  $B_1^+$  power ( $B_1^{\max} = 13.5 \mu\text{T}$ ) and a whole body SAR  $< 2.0 \text{ W/kg}$ . For all pulses the peak amplitude,  $\omega_{\max}$ , was fixed to 500 Hz, in line with commonly used spin-locking amplitudes at 3T.<sup>10</sup> This yields a RAFF pulse reference duration of  $T_{p,\text{RAFF}} = 2.83 \text{ ms}$ .

First, the pulse performance of RAFF was calculated for a visualization region with off-resonances  $\Delta\omega_1^{\text{off}} \in [-400; 400] \text{ Hz}$  and relative  $B_1^+$  scaling factors  $\eta_1 \in [0, 1]$ .

Next, the pulse performance of girRAFF was studied in the presence of field inhomogeneities. To find the

girRAFF parameter combination with optimal resilience against field inhomogeneities the average preparation efficiency ( $\Phi$ ) was calculated over a design region of  $\Delta\omega_1^{\text{off}} \in [-400; 400] \text{ Hz}$  off-resonance and  $\eta_1 \in [0.5, 1]$   $B_1^+$  scaling for different  $\theta$ ,  $\nu$ , and  $\rho$  in the three-dimensional girRAFF parameter space ( $(\theta, \nu, \rho) \in [0^\circ, 5^\circ, \dots, 180^\circ] \times [0, 0.01, \dots, 10] \times [0, 0.01, \dots, 10]$ ). Low magnetization trajectory length ( $< 3.2\pi \text{ rad}$ ) cases were discarded to avoid idle parameter configurations yielding low power pulses with high preparation efficiency but no SL relaxation. The parameter combination  $(\theta, \nu, \rho)$  resulting in the best pulse performance was selected as the optimal girRAFF design for further investigation. Similarly to RAFF, the performance of the optimal girRAFF design was analyzed across a visualization region with off-resonances  $\Delta\omega_1^{\text{off}} \in [-400; 400] \text{ Hz}$  and relative  $B_1^+$  scaling factors  $\eta_1 \in [0, 1]$ .

## 2.3 | Imaging

Imaging was performed on a 3T scanner (Ingenia, Philips). All subjects provided written, informed consent prior to participation in this research study.

### 2.3.1 | Pulse performance in phantom

Simulation results of  $B_0$  and  $B_1^+$  performances for both RAFF and the optimized girRAFF were validated with phantom experiments using a bottle phantom (Spectrasyn 4 polyalphaolefin, ExxonMobil Chemical). The preparation efficiencies were tested by modifying the offset frequency  $\Delta\omega_1^{\text{off}} \in [-400, -375, \dots, 400] \text{ Hz}$  and scaling the pulse amplitude by  $\eta_1 \in [0.05, 0.1, \dots, 1.0]$  for each  $\Delta\omega_1^{\text{off}}$  value. The pulse preparation efficiency,  $M_z(T_p)/M_0$ , was estimated as the ratio of two balanced steady-state free-precession images, one with and one without preparation. The low-resolution balanced steady-state free-precession images were obtained with the following imaging parameters: resolution =  $2 \times 2 \text{ mm}^2$ , slice-thickness = 8 mm, FOV =  $204 \times 204 \text{ mm}^2$ , flip-angle =  $70^\circ$ , TE/TR = 1.37/2.7 ms and a SENSE factor of 2. A 4 s gap between the two balanced steady-state free-precession images was applied to allow for longitudinal magnetization recovery (phantom  $T_1 \approx 242 \text{ ms}$ ). Phase images were used to extract the signal polarity.

### 2.3.2 | $T_{\text{RAFF}}$ and $T_{\text{girRAFF}}$ mapping

In phantom, in vivo calf muscle and knee cartilage  $T_{\text{RAFF}}$  and  $T_{\text{girRAFF}}$  relaxation time mapping were performed

by acquiring five spoiled gradient echo baseline images: one with no preparation, three preceded by a (gir)RAFF preparation and the final one preceded by a saturation preparation. The saturation-prepared image was used to capture the effect of the imaging readout<sup>31</sup> (Figure 1A). 10, 20, and 30 RAFF pulses or 1, 2, and 4 girRAFF pulses were concatenated to obtain preparation modules with varying durations. The pulse repetitions were interspersed with 3 ms spoiler gradients to suppress stimulated echos and aggravating excitation by off-resonance effects. After each readout, a 3 s gap was applied to allow for longitudinal magnetization recovery. All scans shared the following imaging parameters: resolution =  $0.8 \times 0.8$  mm<sup>2</sup>, slice-thickness = 3 mm, FOV =  $181 \times 181$  mm<sup>2</sup>, flip-angle = 15°, number of shots = 6, and a SENSE factor of 2. The TE/TR was 2.5/7.9 ms, 2.4/7.8 ms, and 1.94/6.7 ms for phantoms, calf, and knee cartilage imaging, respectively.

$T_{\text{RAFF}}$  and  $T_{\text{girRAFF}}$  relaxation time maps were obtained in MATLAB (MathWorks) by fitting the following three-parameter model,<sup>31</sup> to account for the readout effect of the imaging pulses:

$$S(t) = A \cdot e^{-\frac{t}{T_{\text{(gir)RAFF}}}} + B. \quad (7)$$

### 2.3.3 | $T_{\text{RAFF}}$ and $T_{\text{girRAFF}}$ relaxation times

RAFF and girRAFF relaxation times obtained in the  $T_1$  Mapping and ECV Standardization in cardiovascular magnetic resonance (TIMES) phantom were compared to conventional  $T_1$  and  $T_2$  times. The optimal girRAFF configuration was used for  $T_{\text{(gir)RAFF}}$  mapping.  $T_{\text{RAFF}}$  and  $T_{\text{girRAFF}}$  values were extracted for each vial of the TIMES phantom using manually drawn circular regions of interest (ROIs). Their mean and SD values were computed for 10 repetitions. The mean  $T_{\text{RAFF}}$  and  $T_{\text{girRAFF}}$  values were compared with reference  $T_1$  and  $T_2$  values reported in Captur et al.<sup>32</sup> via linear regression analysis.  $p$ -values < 0.05 were considered to be statistically significant.

### 2.3.4 | Parameter space evaluation

The effect of design parameter changes in (gir)RAFF was studied in phantom (TIMES<sup>32</sup>) and the calf muscle of four healthy subjects (three males and one female,  $26.5 \pm 2.1$  year old).  $T_{\text{girRAFF}}$  maps were acquired by independently varying each parameter while keeping the other two parameters fixed at the original RAFF value ( $\theta = 0^\circ$ ,  $\nu = 1$ , and  $\rho = 1$ ).  $\theta$ ,  $\nu$  and  $\rho$  were varied across the following ranges:  $\theta = [0^\circ, 18^\circ, \dots, 180^\circ]$ ,  $\nu = [0, 1, 2, 3, \dots, 10]$  and  $\rho = [0, 1, 2, \dots, 10]$ , respectively. Moreover, maps were acquired for  $(\rho, \nu)$ , with  $\rho = \nu\sqrt{2}$

and  $\nu = [1, 1.75, 2.5, \dots, 7]$ , corresponding to the 1-degree of freedom space where the optimal girRAFF solution was found, as illustrated in Figure S4. In the TIMES phantom experiments, relaxation times were evaluated using a circular ROI manually drawn in the vial that most closely resembles the RAFF/girRAFF relaxation times of the muscle tissue. In vivo, ROIs were manually drawn in the central part of the calf muscle.

### 2.3.5 | $B_0$ and $B_1^+$ resilience

The effects of off-resonance and  $B_1^+$  inhomogeneity on the mapping performance were investigated in isolation. To this end, acquisitions were performed in the TIMES phantom (three repetitions) and in the calf muscle of three healthy subjects (two males and one female,  $24.8 \pm 3.0$  year old). For each pulse, maps were acquired at 13 off-resonance frequencies  $\Delta\omega_1^{\text{off}} = [-300, -250, \dots, 300]$  Hz in a first experiment and for 10 relative  $B_1^+$  inhomogeneities  $\eta_1 = [0.1, 0.2, \dots, 1]$  in a second experiment. The  $B_0/B_1^+$  resilience of both pulses was quantified as the range of  $B_0/B_1^+$  inhomogeneities for which less than 10% deviation in the relaxation time from the on-resonant case was observed.

Next, mapping performance was measured for a combination of  $B_0$  and  $B_1^+$  field inhomogeneities, covering the range of inhomogeneities reported for knee cartilage imaging at 3T<sup>33</sup>:  $\Delta\omega_1^{\text{off}} \in \{-150, 0, 150\}$  Hz for each  $\eta_1 \in \{0.5, 0.75, 1.0\}$ . Two sets of experiments were performed. In the first set, RAFF and girRAFF were compared with comparable preparation duration ( $T_{\text{prep, RAFF}} = 28.3, 56.6, 84.9$  ms,  $T_{\text{prep, girRAFF}} = 22.2, 44.3, 88.6$  ms). In the second set, RAFF was performed with shorter preparations ( $T_{\text{prep, RAFF}} = 16.5, 34.0, 67.9$  ms), to account for the shorter in vivo  $T_{\text{RAFF}}$  relaxation times. For each pulse, nine maps were obtained in the TIMES phantom, in the calf muscle of one healthy subject (first set: male, 28 year old, second set: female, 24 year old) and the knee cartilage of another healthy subject (first set only: male, 27 year old). Imaging parameters were the same as described in Section 2.3.2, except for the second set of phantom and calf maps, where a half-scan factor of 0.6 was used to speed up the acquisition. For phantom and calf maps ROIs were manually drawn. For the knee cartilage, relaxation times were assessed in manually drawn ROIs containing the central articular cartilage. The resilience against field inhomogeneities of  $T_{\text{(gir)RAFF}}$  mapping was assessed with three cases: the ideal case ( $I_0$ :  $\eta_1 = 1$ ,  $\Delta\omega_1^{\text{off}} = 0$  Hz), an off-resonance case ( $I_{B_0}$ :  $\eta_1 = 1$ ,  $\Delta\omega_1^{\text{off}} = 150$  Hz), and an imperfect  $B_1^+$  case ( $I_{B_1}$ :  $\eta_1 = 0.5$ ,  $\Delta\omega_1^{\text{off}} = 0$  Hz). The variability of the phantom, calf muscle and knee cartilage relaxation times

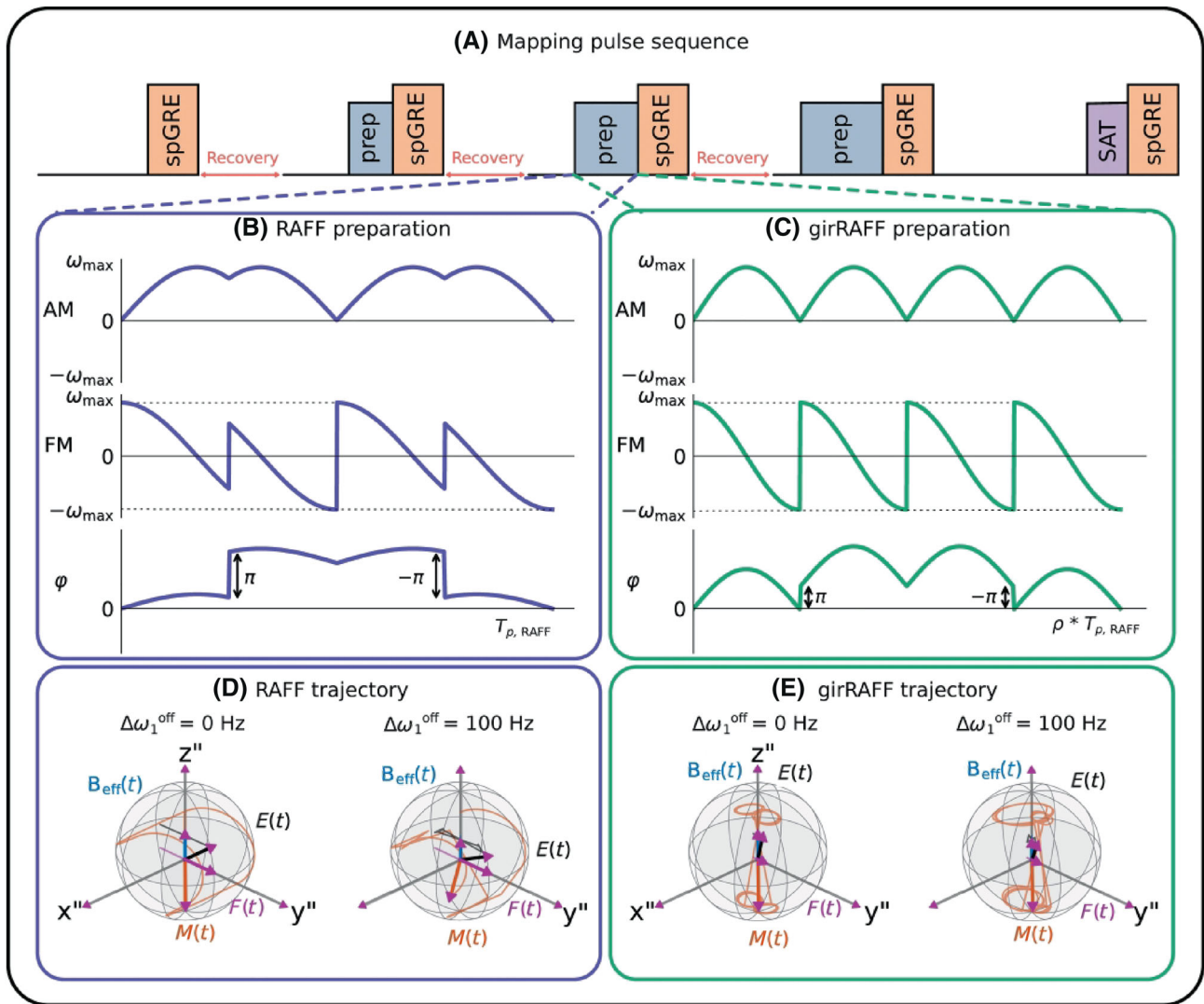


**FIGURE 1** (A) Schematic representation of the  $T_{(gir)RAFF}$  mapping sequence comprising a baseline image with no preparation, three  $T_{(gir)RAFF}$ -prepared images with increasing durations and one saturation-prepared image, interleaved by magnetization recovery delays. (B, C) Radiofrequency (RF) pulse shapes: amplitude modulation (AM), frequency modulation (FM), and phase for both (B) RAFF ( $\theta = 0^\circ$ ,  $\nu = 1$  and  $\rho = 1$ ) and (C) girRAFF ( $\theta = 0^\circ$ ,  $\nu = 5.53$  and  $\rho = 7.82$ ). (D, E)  $M$  (orange) trajectory during RAFF and girRAFF pulses in the second RFR, displayed over a Bloch sphere. The first RFR effective field  $B_{eff}(t)$ , the fictitious field  $F(t)$ , and the second RFR effective field  $E(t)$  are also illustrated. Plots are included for the ideal on-resonance case ( $\Delta\omega_1^{off} = 0$  Hz) and for a simulated off-resonance value  $\Delta\omega_1^{off} = 100$  Hz. Increased off-resonance resilience for girRAFF is indicated with better alignment of  $M$  with the  $z''$ -axis for larger off-resonances.

was assessed using the following metrics: (1) relative difference between the on-resonance case  $\Delta\omega_1^{off} = 0$  Hz and  $\Delta\omega_1^{off} = 150$  Hz  $\left( \Delta I|_{\Delta B_0} = \left| \frac{2(I_0 - I_{B_0})}{I_0 + I_{B_0}} \right| \right)$  and (2) relative difference across  $B_1^+$  conditions  $\left( \Delta I|_{\Delta B_1} = \left| \frac{2(I_0 - I_{B_1})}{I_0 + I_{B_1}} \right| \right)$ . Each metric was computed based on average  $T_{RAFF}$  and  $T_{girRAFF}$  intensities  $I$  extracted from the corresponding ROIs.

In a second cohort of five healthy subjects (four males, one female,  $27.4 \pm 3.1$  year old), girRAFF and RAFF mapping was performed in the knee cartilage using Dixon fat-water separation to exclude the effect of adipose

tissue on  $B_0$  and  $B_1^+$  resilience. Dixon imaging was performed with a multi-echo acquisition (three echoes,  $\Delta TE = 2.5$  ms), and the following imaging parameters: resolution =  $0.9 \times 0.9$  mm<sup>2</sup>, slice-thickness = 3 mm, FOV =  $181 \times 181$  mm<sup>2</sup>, flip angle =  $15^\circ$ , number of shots = 3, SENSE factor = 2, TE/ $\Delta TE$ /TR = 1.93/1.5/6.9 ms. Imaging was performed for a single slice in the lateral section of the knee articulation of each subject (three left knee, two right knee). Artificial off-resonance of  $\Delta\omega_1^{off} = [-150, -75, \dots, 150]$  Hz was additionally induced. Fat-suppressed  $T_{RAFF}$  and  $T_{girRAFF}$  relaxation maps were generated from the water-only images obtained with a 3-point Dixon reconstruction. Robustness against  $B_0$

inhomogeneities was compared for the fat-suppressed maps and maps without fat-suppression obtained from the first echo of the Dixon scan. To this end, the relative difference between the on-resonance  $\Delta\omega_1^{\text{off}} = 0$  Hz and off-resonance cases  $\Delta\omega_1^{\text{off}} = [-150, -75, 75, 150]$  Hz was used  $\left( \Delta I |_{\Delta B_0} = \frac{1}{4} \sum_{B_0=[-150, -75, 75, 150]} \left| \frac{2(I_0 - I_{B_0})}{I_0 + I_{B_0}} \right| \right)$ . Mann–Whitney  $U$ -tests were used to assess the statistical significance of differences between RAFF/girRAFF performance metrics with and without fat suppression.

### 2.3.6 | In vivo reproducibility

Inter-slice reproducibility was investigated by acquiring five on-resonance sagittal slices (slice gap = 3 mm) of the knee cartilage for each subject. All scans were acquired in a cohort of five healthy volunteers (three males and two females,  $25.2 \pm 2.7$  year old). The same imaging parameters as for the above-listed in vivo acquisitions were used for this cohort, except for a longer recovery time between each shot (4 s) to improve quantification accuracy.

The reproducibility of the knee cartilage relaxation times was assessed using the inter-subject variability ( $\text{CoV}_{\text{subject}}$ ) and the inter-slice ( $\text{CoV}_{\text{slice}}$ ) coefficients of variation. Mann–Whitney  $U$ -tests were used to assess the statistical significance of differences between RAFF and girRAFF performance metrics,  $p < 0.05$  was considered statistically significant.

## 3 | RESULTS

### 3.1 | Bloch simulations

Figure 2A shows the RAFF performance plots for  $(\eta_1, \Delta\omega_1^{\text{off}}) \in [0, 1] \times [-400, 400]$  Hz in simulations. Here, RAFF preparations present moderate resilience against  $B_0$  inhomogeneities, with a bandwidth of 318 Hz for a 10% tolerance threshold. Figure 2B shows the pulse performance for girRAFF with parameters  $\theta = 0^\circ$ ,  $\nu = 5.53$ ,  $\rho = 7.82$ . With these parameters, girRAFF has an increased off-resonance bandwidth (536 Hz) yielding a larger homogeneous pulse performance compared with RAFF. The average preparation efficiency  $\Phi$  over the design window (dashed black rectangle in Figure 2A,B) is considerably higher for girRAFF ( $\Phi = 0.95$ ) preparations than for RAFF ( $\Phi = 0.36$ ).

Figure 3A depicts the average pulse performance across the inhomogeneity design region for various girRAFF pulses in the three-dimensional parameter space.

Preparation efficiency and magnetization trajectory length are depicted in Figure 3C,D for the two-dimensional planes in the parameter space intersecting with the original RAFF pulse parameters ( $\theta = 0^\circ$ ,  $\nu = 1$  and  $\rho = 1$ ). All cross-sectional plots indicate an increased  $\Phi$  for small preparation duration factors  $\rho$  and small values of  $\nu$ . Simultaneously, however, the magnetization trajectory length drops substantially for small  $\rho$  and  $\nu$  (Figure 3C,D, left and middle), indicating no effective spin-locking behavior caused by reduced effective field amplitudes. A pattern of high preparation efficiency and trajectory length is observed for  $\rho = \nu\sqrt{2}$  (Figure 3C,D, middle). Improved performance is also shown for higher harmonics ( $\rho = n\sqrt{2}\nu$ ,  $n = 2, 3, \dots$ ). The optimal combination of parameters for girRAFF is found for  $\theta = 0^\circ$ ,  $\nu = 5.53$  and  $\rho = 7.82$  with  $\rho \approx \sqrt{2}\nu$ .

### 3.2 | Pulse performance in phantom

Figure 2C,D depicts the experimental validation of the simulated pulse performances for the same  $B_0$  and  $B_1^+$  range. The averaged preparation efficiencies over the design region are  $\Phi = 0.67$  for RAFF and  $\Phi = 0.91$  for girRAFF, confirming the improvement in robustness for girRAFF over RAFF observed in simulations. In visual inspection, the simulated RAFF pulse performance closely matches the hyperbolic shape observed in the phantom experiments, also exhibiting a comparable bandwidth. Similarly, good agreement between simulations and phantom experiments is visually apparent for girRAFF. The location of the low-resolution speckle structure for low  $\eta_1$  values agrees well between simulation and phantom performance.

#### 3.2.1 | $T_{\text{RAFF}}$ and $T_{\text{girRAFF}}$ relaxation times

Figure S6 shows the  $T_{\text{RAFF}}$  and  $T_{\text{girRAFF}}$  trends as a function of  $T_1$  (Figure S6A) and  $T_2$  (Figure S6B) in the TIMES phantom vials.  $T_{\text{girRAFF}}$  values are consistently higher than  $T_{\text{RAFF}}$ . The relaxation times in the central phantom vial are measured as  $T_{\text{RAFF}} = 62 \pm 14$  ms and  $T_{\text{girRAFF}} = 71 \pm 16$  ms, respectively. Linear regression analysis yields that neither  $T_{\text{RAFF}}$  nor  $T_{\text{girRAFF}}$  are linearly dependent on  $T_1$  ( $T_{\text{RAFF}}$  vs.  $T_1$ :  $R^2 = 0.001$ ,  $p = 0.94$ ,  $T_{\text{girRAFF}}$  vs.  $T_1$ :  $R^2 = 0.09$ ,  $p = 0.44$ ). While a linear dependence is observed for both RAFF and girRAFF as a function of  $T_2$  ( $T_{\text{RAFF}}$  vs.  $T_2$ :  $R^2 = 0.87$ ,  $p < 10^{-3}$ ,  $T_{\text{girRAFF}}$  vs.  $T_2$ :  $R^2 = 0.99$ ,  $p < 10^{-8}$ ), differential behavior is still observed, particularly for short  $T_2$  times.

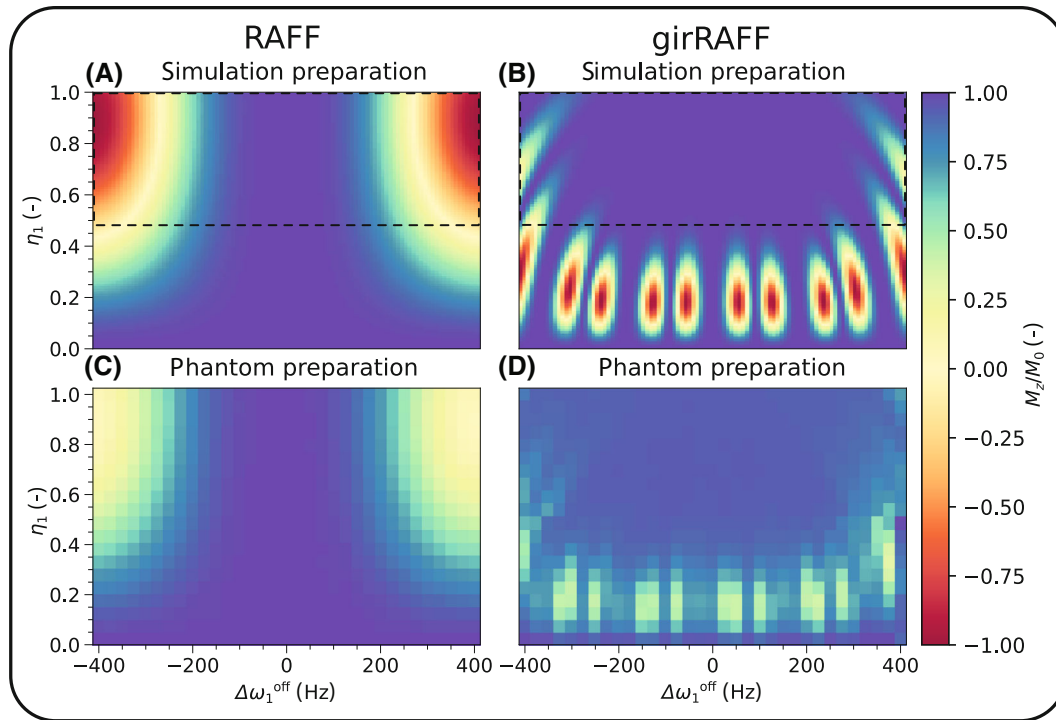


**FIGURE 2** Preparation efficiency ( $M_z/M_0$ ) obtained with relaxation along a fictitious field (RAFF) (A, C) and generalized inhomogeneity-resilient RAFF (girRAFF) (B, D) pulses for  $(\eta_1, \Delta\omega_1^{\text{off}}) \in [0, 1] \times [-400, 400]$  Hz in simulations (top) and in phantom experiments (bottom). Here  $\Delta\omega_1^{\text{off}}$  indicates the off-resonance value and  $\eta_1$  is the ratio between the effective and nominal  $B_1^+$  power. The dashed rectangle indicates the design region used for pulse optimization. In simulations, an average of 0.36 and 0.95 was measured for RAFF, and girRAFF, respectively. In the phantom, a single RAFF preparation of 2.83 ms resulted in an averaged  $M_z$  of 0.67 and a single girRAFF preparation ( $7.82 T_{p,\text{RAFF}}$ ) resulted in an average of 0.91 for the upper half-plane. Improved resilience against field inhomogeneities is obtained for girRAFF compared to RAFF, shown in the enlarged off-resonance bandwidth for the homogeneous performance plane close to 1.

### 3.3 | Parameters space evaluation

Figure 4 shows the  $T_{\text{girRAFF}}$  relaxation times across various parameter changes in the phantom and in the calf muscle. The parametric change of  $\theta$  (Figure 4A) demonstrates a cyclic behavior with a maximum around  $\theta \approx \pi/4$  and a minimum around  $\theta \approx 3\pi/4$  both in phantom and in vivo. Changes in  $\rho$  lead to only minor alteration in  $T_{\text{girRAFF}}$ , except for  $\rho = 1$  (Figure 4B). For the parametric change of  $\nu$ , increasing relaxation times are obtained for increased  $B_{\text{eff}}(t)$  strength relative to  $F(t)$ , both in the phantom and calf, except for  $\nu = 0$  (Figure 4C). Finally, the parametric change for  $\rho = \nu\sqrt{2}$ , in Figure 4D, shows only minor changes in  $T_{\text{girRAFF}}$  for increasing  $\rho$  and  $\nu$ .

### 3.4 | $B_0$ and $B_1^+$ resilience

Figure 5, shows the field inhomogeneities performances of RAFF and girRAFF, studied individually with dense  $\eta_1$  and  $\Delta\omega_1^{\text{off}}$  sampling. For phantom and in vivo calf mapping, on-resonance maps with the manually drawn ROIs containing a vial or muscle tissue are shown in

Figure 5A,B, respectively. For both, the calf and phantom,  $T_{\text{girRAFF}}$  shows less than  $\pm 10\%$  deviation over a large range of off-resonances (bandwidth =  $447 \pm 31$  Hz in phantom,  $496 \pm 14$  Hz in the calf), while  $T_{\text{RAFF}}$  times are marked with large deviations in the presence of smaller off-resonances (bandwidth =  $74 \pm 23$  Hz in phantom,  $104 \pm 8$  Hz in the calf). For both pulses, a  $B_0$  shift of approximately 50 Hz off the center frequency is visible, likely due to imperfect shimming. For relative  $B_1^+$  performance, RAFF exhibits increased relaxation times at decreased effective  $B_1^+$  and exceeds the  $\pm 10\%$  bound for  $\eta_1 < 0.89$  (SD = 0.04) for both phantom and calf. girRAFF remains within the tolerance for a larger range,  $0.48 \leq \eta_1 \leq 1$  (SD = 0.01) and  $0.42 \leq \eta_1 \leq 1$  (SD = 0.03), in the phantom and calf, respectively. Thus, girRAFF yielded 6.04 $\times$  (phantom) or 4.77 $\times$  (calf muscle) larger  $B_0$  bandwidth than RAFF, as well as 4.73 $\times$  (phantom) or 5.27 $\times$  (calf muscle) better resilience to  $B_1^+$  inhomogeneities.

In Figure 6A,B, the first set of phantom girRAFF and RAFF maps, acquired with comparable RAFF and girRAFF preparation durations, for nine different  $B_0$  and  $B_1^+$  inhomogeneity combinations are shown. For the on-resonant case ( $\eta_1 = 1, \Delta\omega_1^{\text{off}} = 0$  Hz), the relaxation

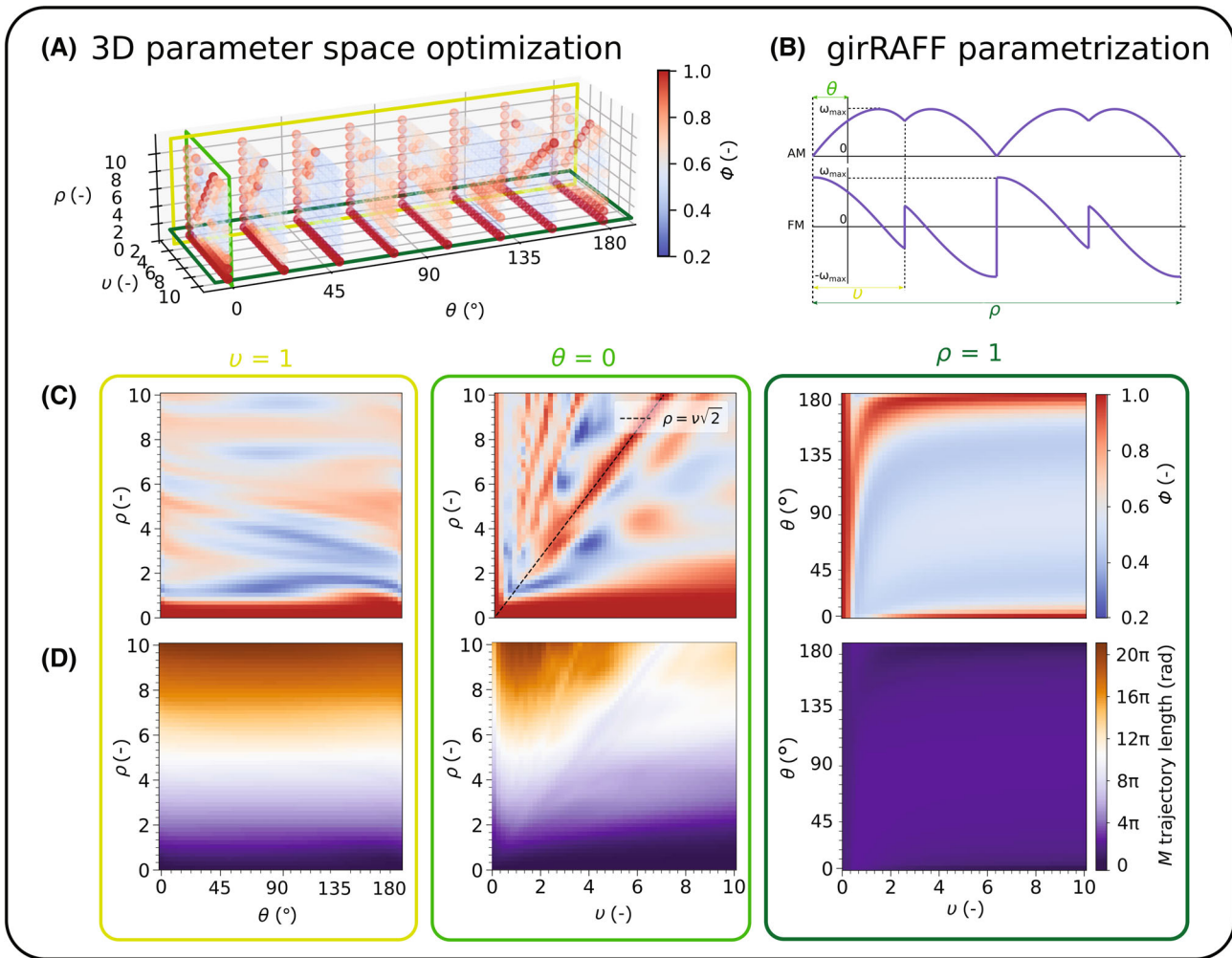


**FIGURE 3** (A) Visualization of the pulse efficiency for the generalized inhomogeneity-resilient RAFF (girRAFF) three-dimensional parameter space within the bounds:  $(\theta, \nu, \rho) \in [0^\circ, 180^\circ] \times [0, 10] \times [0, 10]$ . The pulse peak power ( $\omega_{\max}$ ) was fixed to 500 Hz. For each parameter combination, the preparation efficiency  $M_z/M_0$  was averaged over the region  $(\eta_1, \Delta\omega_1^{\text{off}}) \in [0.5, 1] \times [-400, 400]$  Hz. The optimal shape parameters, identified by an exhaustive search of the parameter grid for the maximum  $\Phi$ , while maintaining a magnetization trajectory length above 10, were  $\theta = 0^\circ$ ,  $\nu = 5.53$  and  $\rho = 7.82$ . (B) Schematic representation of  $\theta$ ,  $\nu$ , and  $\rho$  parameters effect on the girRAFF pulse shape. (C) Two-dimensional preparation efficiency and (D) Trajectory length maps, obtained by fixing one parameter at a time ( $\theta = 0$  in the center,  $\nu = 1$  on the left, and  $\rho = 1$  on the right). All two-dimensional plots indicated an increased averaged  $M_z$  for small values of  $\rho$  and  $\nu$ , which was accompanied by a dramatic drop in trajectory length.

times in the muscle-like vial are measured as  $T_{\text{RAFF}} = 74 \pm 2$  ms and  $T_{\text{girRAFF}} = 98 \pm 3$  ms, respectively. Visually consistent mapping quality is obtained for girRAFF across the studied range of  $B_0$  and  $B_1^+$  inhomogeneities, with only minor differences between the off-resonance and  $\eta_1$  values. RAFF mapping yields larger fluctuations in the measured relaxation time for all studied field inhomogeneities. Similar results are shown in the  $T_{(\text{gir})\text{RAFF}}$  maps of the calf muscle acquired in the presence of artificially induced field inhomogeneities (Figure 6C,D). The average relaxation time in the selected ROI is  $T_{\text{RAFF}} = 34 \pm 1$  ms and  $T_{\text{girRAFF}} = 50 \pm 1$  ms at on-resonance. Across  $B_0$  field inhomogeneities, RAFF has a  $\Delta I|_{\Delta B_0}$  of 48.2% and 56.3% in the phantom and calf, respectively. girRAFF shows increased

consistency with  $\Delta I|_{\Delta B_0}$  of 6.3% in the phantom and 7.9% in the calf. Resilience to  $B_1^+$  inhomogeneities is also higher for girRAFF ( $\Delta I|_{\Delta B_1} = 9.4\%$  in phantom, 12.2% in the calf) than for RAFF ( $\Delta I|_{\Delta B_1} = 45.7\%$  in phantom, 49.1% in the calf).

Phantom and calf girRAFF and RAFF maps obtained in the second set of experiments are shown in the Supporting Information Figure S7. Here adapted RAFF preparation durations are used to achieve comparable exponential decay fractions between RAFF and girRAFF. Mildly improved resilience to  $B_0$  and  $B_1^+$  inhomogeneities is observed using adapted RAFF preparations ( $\Delta I|_{\Delta B_0} = 40.6\%$  in phantom, 45.8% in the calf,  $\Delta I|_{\Delta B_1} = 42.3\%$  in phantom, 41.8% in the calf) compared to the  $T_{\text{RAFF}}$

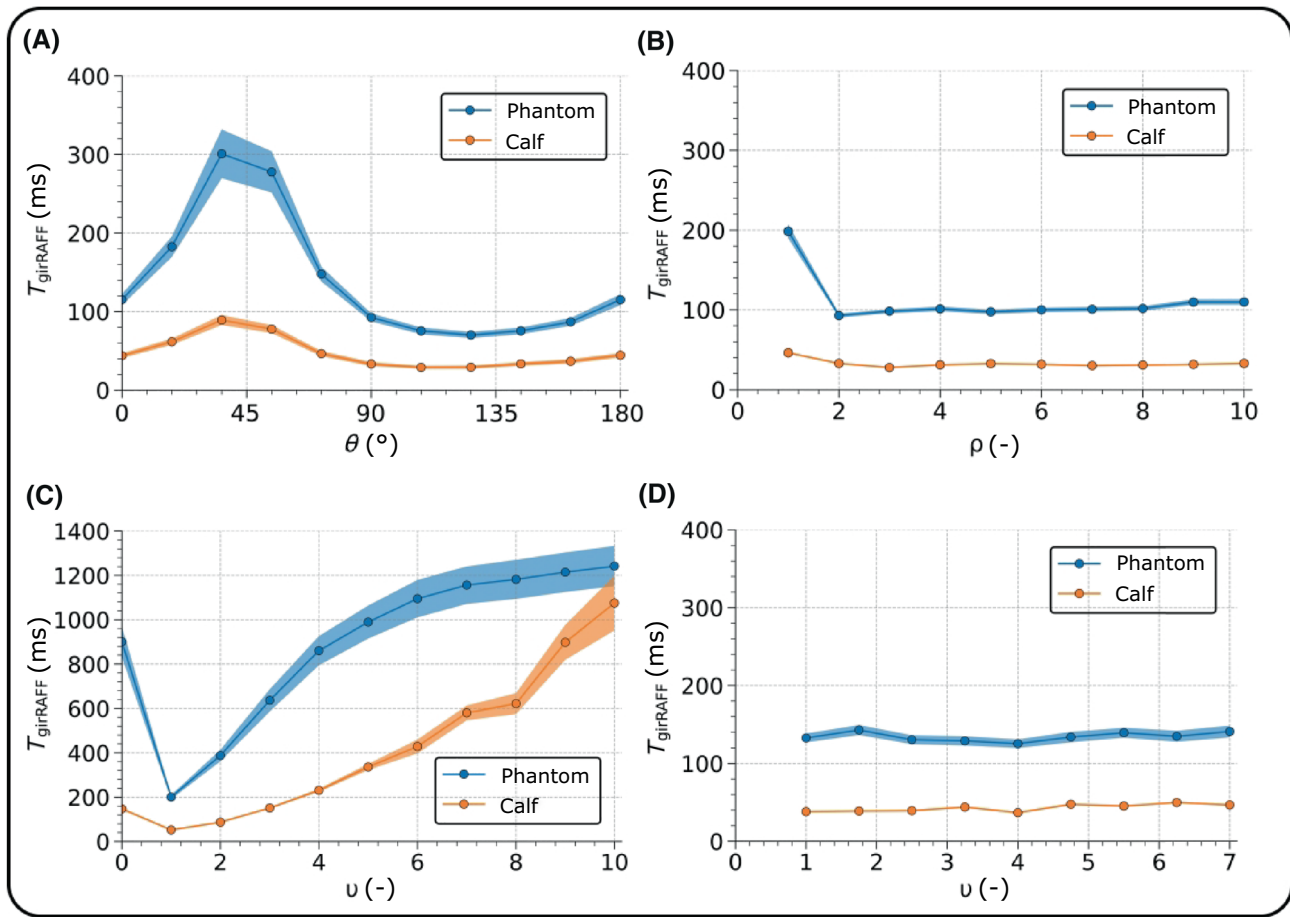


**FIGURE 4** Quantitative assessment of  $T_{\text{girRAFF}}$  for (A)  $\theta \in \{0, 18^\circ, \dots, 180^\circ\}$ , (B)  $\rho \in \{0, 1, 2, \dots, 10\}$  and (C)  $\nu \in \{0, 1, 2, \dots, 10\}$  in the T1MES<sup>32</sup> phantom (blue) and in the calf muscle (orange).  $T_{\text{girRAFF}}$  dependency on the pulse parameters is also investigated for  $\rho = \nu\sqrt{2}$  with  $\nu \in \{1, 1.75, 2.5, \dots, 7\}$ , along which the optimal combination of girRAFF parameters is found. Phantom and calf results show good agreement for the investigated parameters.

maps obtained in the first set. However, even with adapted preparation delays the resilience of RAFF against off-resonances is still  $\approx 4.8$  times lower than for girRAFF in phantom and  $\approx 4.3$  times in the calf. Similarly, the resilience to  $B_1^+$  inhomogeneities is  $\approx 5.0$  lower in the phantom and  $\approx 4.7$  times in the calf.

$T_{\text{RAFF}}$  and  $T_{\text{girRAFF}}$  relaxation maps, acquired for different combinations of  $B_0$  and  $B_1^+$  inhomogeneities in the knee cartilage are depicted in Figure 7A,B.  $T_{\text{RAFF}} = 42 \pm 11$  ms  $T_{\text{girRAFF}} = 53 \pm 14$  ms are found in the knee cartilage for the on-resonance condition. Higher variability can be observed for  $T_{\text{RAFF}}$  maps across inhomogeneity conditions compared with  $T_{\text{girRAFF}}$ . The  $\Delta I|_{\Delta B_0}$  scores, averaged across the 5 subjects, are significantly higher for RAFF ( $\Delta I|_{\Delta B_0} = 61\%$ ) than girRAFF ( $\Delta I|_{\Delta B_0} = 8\%$ ,  $p < 10^{-3}$ ), as shown in Figure 7C,D. Similarly, the RAFF pulse is significantly less resilient against  $B_1^+$  inhomogeneities ( $\Delta I|_{\Delta B_1} = 54\%$  for RAFF, 11% for girRAFF,  $p < 10^{-3}$ ), as shown in Figure 7A,B.

The comparison of  $T_{\text{RAFF}}$  and  $T_{\text{girRAFF}}$  knee cartilage maps obtained with and without Dixon fat-suppression for five different values of  $B_0$  inhomogeneities ( $\Delta\omega_1^{\text{off}}$ ) is shown in Figure 8.  $T_{\text{RAFF}}$  maps acquired both with and without fat suppression display high variability in the presence of  $B_0$  inhomogeneities ( $\Delta I|_{\Delta B_0} = 40\%$  without fat suppression,  $\Delta I|_{\Delta B_0} = 47\%$  with Dixon fat suppression,  $p < 10^{-2}$ ). Specifically,  $T_{\text{RAFF}}$  values show a trend of substantial reduction for increasing  $|\Delta\omega_1^{\text{off}}|$ . The influence of adipose tissue in the proximity of the knee cartilage creates areas of enhanced  $T_{\text{RAFF}}$  which partially balance the trend of decreasing  $T_{\text{RAFF}}$  for increasing  $|\Delta\omega_1^{\text{off}}|$ , leading to a reduced  $\Delta I|_{\Delta B_0}$  coefficient. On the other hand, girRAFF maps show overall more homogeneous values across different  $\Delta\omega_1^{\text{off}}$  conditions. However, localized hyperenhancement is visible in the proximity of adipose tissue in the knee joint, especially for  $\Delta\omega_1^{\text{off}} > 0$  Hz (red arrows in Figure 8B). These regions of hyperenhancement are visibly suppressed with the use of Dixon fat-water separation. As

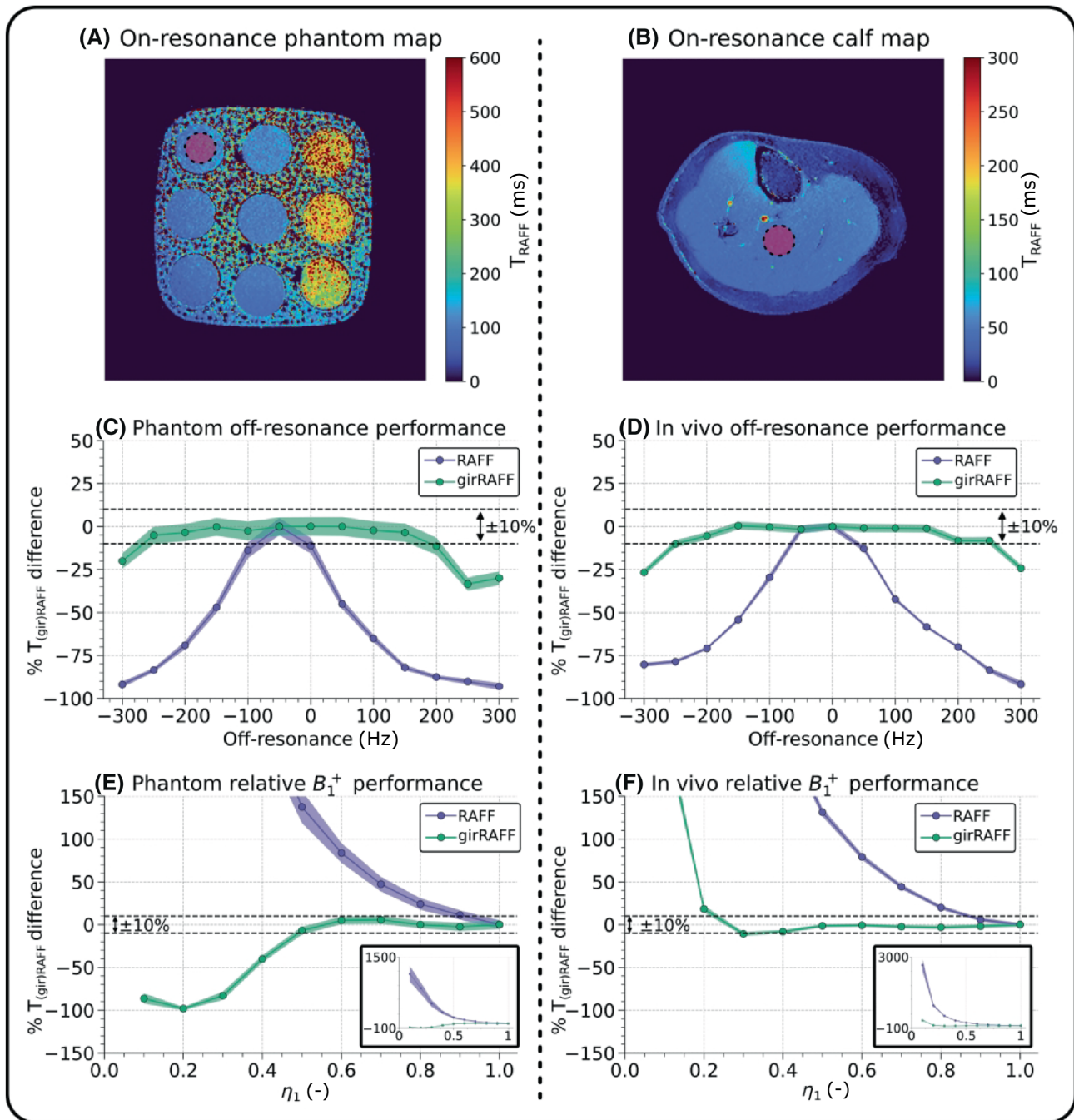


**FIGURE 5** (A,B) Phantom and in vivo calf relaxation along a fictitious field (RAFF) maps, respectively. For RAFF and generalized inhomogeneity-resilient RAFF (girRAFF), a circular region of interest (ROI) containing a vial or muscle tissue was selected to assess relaxation time for different off-resonance ( $\Delta\omega_1^{\text{off}}$ ) and relative  $B_1^+$  ( $\eta_1$ ) values. Off-resonance performance of RAFF (blue) and girRAFF (green) (C) in the phantom vial and (D) in the calf muscle for  $\Delta\omega_1^{\text{off}} \in \{-300, -250, \dots, 300\}$  Hz obtained for  $B_{1,\text{max}}^+ = 13.5 \mu\text{T}$ . Relative  $B_1^+$  performance of RAFF and girRAFF (E) in the phantom and (F) the calf muscle for  $\eta_1 \in \{0.1, 0.2, \dots, 1\}$  obtained for  $\Delta\omega_1^{\text{off}} = 0$  Hz. Increased off-resonance and relative  $B_1^+$  resilience is obtained for girRAFF compared with RAFF in the phantom and in the calf.  $T_{\text{girRAFF}}$  oscillations remain lower than 10% for a  $447 \pm 31$  Hz wide frequency range compared with  $74 \pm 23$  Hz for RAFF in the phantom. In vivo, a  $496 \pm 14$  Hz wide frequency range is obtained for girRAFF compared with  $104 \pm 8$  Hz for RAFF. For relative  $B_1^+$  performance,  $T_{\text{girRAFF}}$  the ranges are:  $0.48 \leq \eta_1 \leq 1$  and  $0.42 \leq \eta_1 \leq 1$  in the phantom and calf, respectively.  $T_{\text{RAFF}}$  exceeds the tolerance for  $\eta_1 < 0.89$  for both phantom and calf.

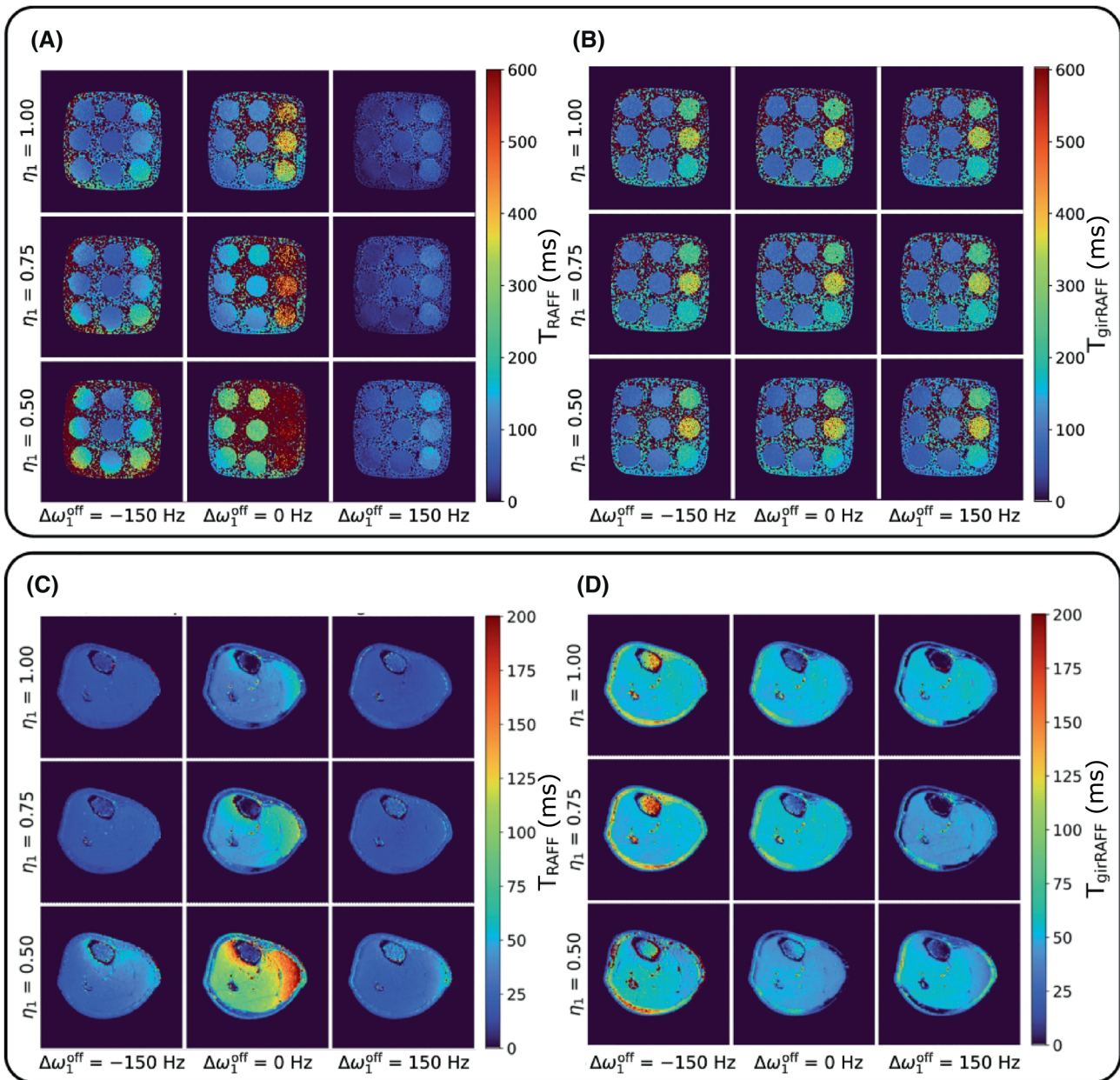


**FIGURE 6** (A,B) Phantom and (C,D) in vivo calf relaxation along a fictitious field (RAFF) and generalized inhomogeneity-resilient RAFF (girRAFF) maps obtained for each combination of  $(\Delta\omega_1^{\text{off}}, \eta_1) \in \{-150, 0, 150\} \text{ Hz} \times \{0.5, 0.75, 1.0\}$ . Both phantom and calf maps show high variability for RAFF preparations across inhomogeneity combinations.  $T_{\text{girRAFF}}$  maps, on the other hand, show good resilience to system imperfections.

a result, fat suppression significantly improves the robustness of  $T_{\text{girRAFF}}$  maps to  $B_0$  inhomogeneities ( $\Delta I|_{\Delta B_0} = 6\%$  without fat suppression,  $\Delta I|_{\Delta B_0} = 0.4\%$  with Dixon fat suppression,  $p < 10^{-8}$ ).

### 3.5 | In vivo reproducibility

Figure 9 displays one of the sagittal slices acquired for all five healthy subjects and an example of the five sagittal

$T_{\text{RAFF}}$  and  $T_{\text{girRAFF}}$  slices for a representative subject. The inter-subject analysis across all field inhomogeneities and slices yields  $\text{CoV}_{\text{subjects}} = 27\%$  for RAFF, while girRAFF shows improved reproducibility with  $\text{CoV}_{\text{subjects}} = 14\%$  ( $p < 10^{-2}$ ). Moreover,  $T_{\text{girRAFF}}$  maps yield homogeneous relaxation times across all slices ( $\text{CoV}_{\text{slice}} = 10\%$ ), whereas  $T_{\text{RAFF}}$  are characterized by higher variability across the five slices ( $\text{CoV}_{\text{slice}} = 16\%$ ,  $p < 0.01$ ), with decreased values in lateral and medial extremities. Moderate relaxation time variations across slices, however, could also be caused

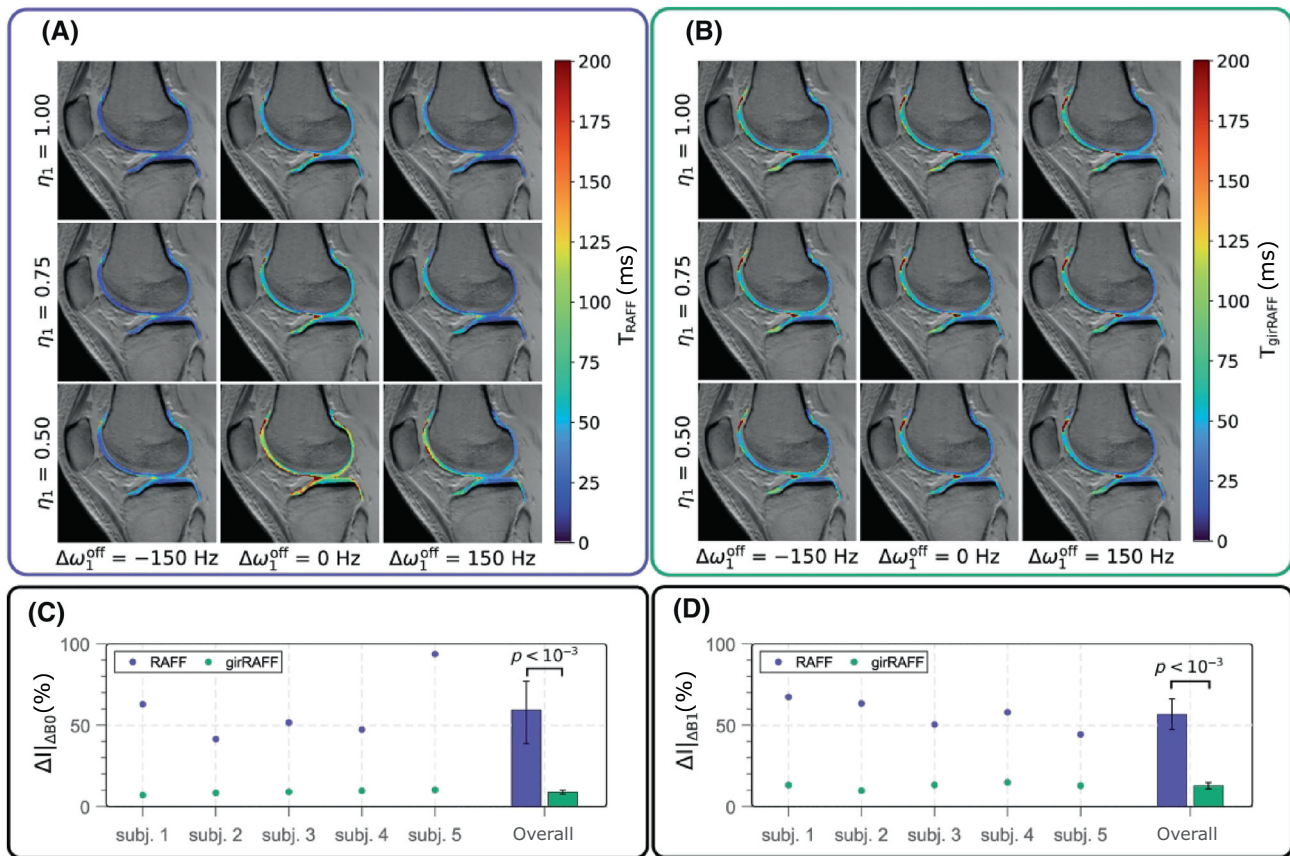


**FIGURE 7** (A,B) In vivo maps, for both relaxation along a fictitious field (RAFF) and generalized inhomogeneity-resilient RAFF (girRAFF), obtained for each combination of  $\Delta\omega_1^{\text{off}} \in \{-150, 0, 150\}$  Hz and  $\eta_1 \in \{0.5, 0.75, 1.0\}$ . Manually segmented cartilage  $T_{\text{RAFF}}$  and  $T_{\text{girRAFF}}$  values are displayed over a baseline image acquired with no preparation. Improved consistency is shown for girRAFF in the knee cartilage, as shown in the plots (C) and (D) illustrating the  $\Delta I|_{\Delta B_0}$  and  $\Delta I|_{\Delta B_1}$ , respectively, for each subject and then averaged over all subjects.

by the intrinsic  $T_{(\text{gir})\text{RAFF}}$  anisotropy, as shown in previous studies,<sup>34,35</sup> as well as differences in partial voluming of the thin ROIs.

## 4 | DISCUSSION

In this work, the resilience of RAFF pulses against field inhomogeneities was investigated. Both simulations and phantom experiments showed strong susceptibility to changes in the  $B_1^+$  field and moderate resilience against off-resonances for RAFF. A parametric formulation of RAFF was introduced to explore pulse shapes that yield constant but nonequal effective and fictitious fields. The resilience of these pulses to  $B_0$  and  $B_1^+$  inhomogeneities was investigated to find the optimal candidate for robust rotating frame relaxation mapping. For the optimal parameters, girRAFF showed 4.77 and 5.27 times increased resilience against  $B_0$  and  $B_1^+$  inhomogeneities in the human calf, respectively, while maintaining good tissue contrast and mapping quality in phantom, calf, and knee cartilage imaging.

RAFF represents an emerging biomarker for tissue characterization and has already proven sensitivity to proteoglycan concentration in articular cartilage, making it a promising candidate for osteoarthritis detection.<sup>36</sup> Previous RAFF mapping studies focused on ex vivo samples or animal models of the knee cartilage and were performed at preclinical systems with ultrahigh field strengths (9.4T).<sup>11,34–38</sup> In healthy subjects at 3T, Tourais et al. recently reported an average of  $T_{\text{RAFF}} = 45.2 \pm 11.3$  ms,<sup>27</sup> which is in close agreement with the values obtained in this study. Optimized girRAFF preparations yield longer relaxation times compared with RAFF, a trend consistent with findings by Liimatainen et al.<sup>21</sup> Specifically, they found a significant dependence of RAFF relaxation times on the ratio between the effective and fictitious field components (equivalent to  $\nu$  in our study). The lowest  $T_{\text{RAFF}}$  values were measured when the effective field strength was almost equal to the fictitious field strength (corresponding to values of  $\nu$  just below 1), whereas higher  $T_{\text{RAFF}}$  values were measured when the effective field was much stronger or much weaker than the fictitious field. This dependence is confirmed by the phantom and in vivo results in Figure 4C.

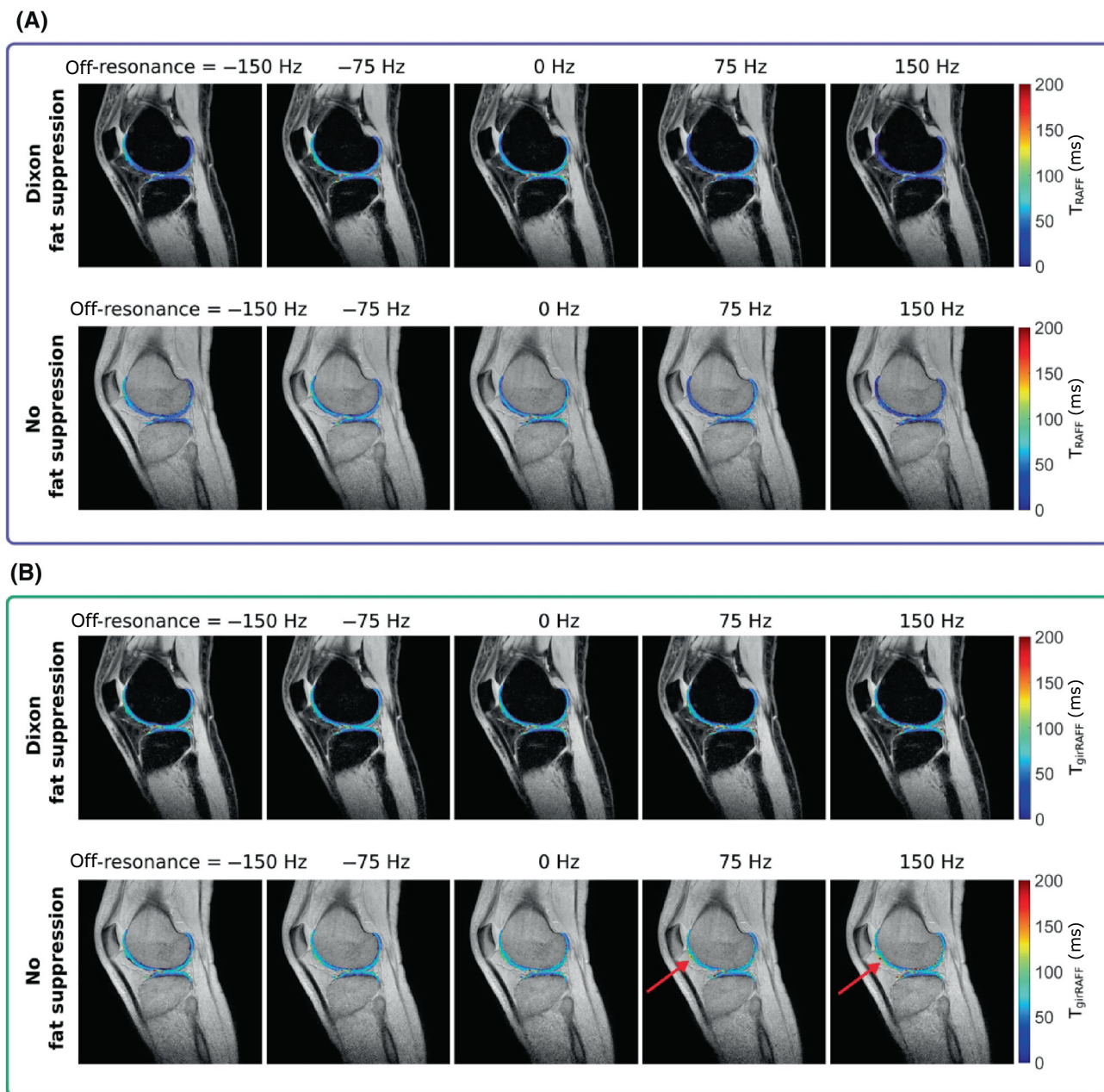


**FIGURE 8** Example  $T_{\text{RAFF}}$  (A) and  $T_{\text{girRAFF}}$  (B) relaxation maps of the articular cartilage, acquired in a healthy subject with Dixon fat-water separation (top) and without fat suppression (bottom), for various artificially induced off-resonance values.  $T_{\text{RAFF}}$  maps show strong variability across the off-resonance conditions with and without fat suppression. The variability is visually reduced in the  $T_{\text{girRAFF}}$  maps. Residual artifacts are observed in the  $T_{\text{girRAFF}}$  maps in areas close to adipose tissue (red arrow). Dixon fat-water separation successfully alleviates these artifacts leading to visually homogeneous maps across the off-resonance conditions.

The variability in the measured  $T_{\text{girRAFF}}$  times for different  $\nu$  hints at differential sensitivity to underlying physical processes such as dipole–dipole interactions or chemical exchange when moving from the sub-adiabatic condition toward an adiabatic regime. Evaluation in patients is warranted to fully characterize the sensitivity of RAFF and girRAFF pulses to underlying tissue composition and their pathological state alterations.

RAFF pulses were originally proposed as an alternative to conventional continuous-wave  $T_{1\rho}$  preparations

for robust rotating frame relaxation quantification with limited SAR burden. As Liimatainen et al. have shown in their original study,  $T_{\text{RAFF}}$  relaxation displays a pattern of sensitivity to molecular motion that is similar to  $T_{1\rho,\text{adiab}}$  and  $T_{2\rho,\text{adiab}}$ ,<sup>20</sup> and related to continuous-wave  $T_{1\rho}$  and  $T_{2\rho}$  relaxation times. Thus, RAFF pulses were proposed as an alternative to conventional continuous-wave rotating frame relaxation techniques with the promise of comparable clinical sensitivity. Initial studies showed a moderate increase in off-resonance bandwidth up to  $\sim 100$

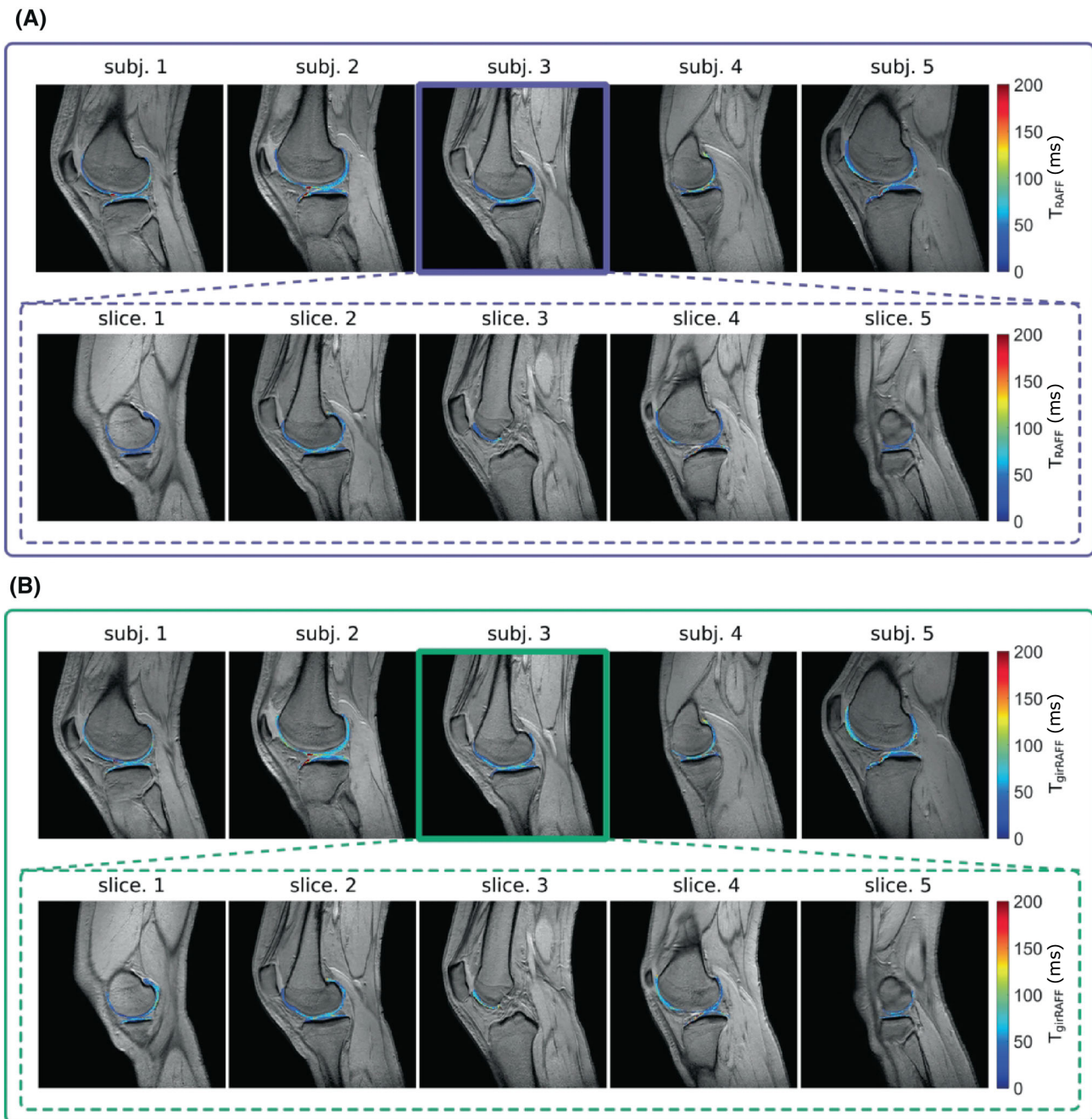


**FIGURE 9** Example of in vivo (A) relaxation along a fictitious field (RAFF) and (B) generalized inhomogeneity-resilient RAFF (girRAFF) maps obtained in the knee cartilage of five healthy subjects. For a representative subject, examples of five different sagittal maps are shown below. Cartilage  $T_{\text{girRAFF}}$  values appear more homogeneous than  $T_{\text{RAFF}}$  across the five subjects ( $\text{CoV}_{\text{subjects}} = 27\%$  for RAFF,  $14\%$  for girRAFF,  $p < 0.01$ ) and 5 slices ( $\text{CoV}_{\text{slices}} = 16\%$  for RAFF,  $10\%$  for girRAFF,  $p < 0.01$ ).

Hz.<sup>20,29</sup> However, this came at the expense of a loss of resilience against  $B_1^+$  field inhomogeneities, with simulated  $T_{\text{RAFF}}$  times significantly impaired for  $\eta_1 < 0.8$ .<sup>20</sup> These results are well in line with the results obtained in this study, where a bandwidth of  $74 \pm 23$  Hz and 10% tolerance to  $B_1^+$  inhomogeneities were measured in phantom for RAFF. In this study, we proposed a RAFF optimization, girRAFF, based on the combined study of both  $B_0$

and  $B_1^+$  inhomogeneities. By relaxing the RAFF condition (Equation 1), introducing 3 degrees of freedom, constant yet not necessarily equal effective and fictitious field components are achieved. In agreement with previous findings,<sup>29</sup> our results show that the average preparation efficiency improved for higher fictitious field ratios ( $\nu < 1$ ). However, even better performances were achieved for  $\nu > 1$ , with the optimal value found for  $\nu = 5.53$ . Increasing

$\nu$  values yield an increasingly strong effective field component with respect to the fictitious field, gradually moving from a sub-adiabatic to an adiabatic regime. Accordingly, the analysis of contrast sensitivity in the presence of dipole–dipole interactions showed that girRAFF falls between the sensitivity profiles of RAFF and  $T_{1\rho, \text{adiab}}$ . Notably, optimal girRAFF performances were observed for configurations where  $\rho = n\sqrt{2}\nu$ . This parameter combination corresponds to cases where the argument of girRAFF amplitude and frequency modulation functions ranges from 0 to  $180^\circ$  within a single P-packet. Thus, the effective field completes a full  $180^\circ$  inversion, leading to increased robustness against field inhomogeneities in the optimization.

Higher rank RAFF pulses (RAFF $n$ , with  $n > 2$ ) were previously proposed as a solution to improve the pulse resilience to  $B_0$  field inhomogeneities.<sup>29</sup> RAFF $n$  pulses generalize the RAFF conditions of equal and time-invariant effective and fictitious field components to higher-order RFRs. Observed in the second RFR, these pulses are characterized by a higher fictitious field component with respect to the effective field. A joint optimization of  $B_0$  and  $B_1^+$  inhomogeneity resilience, as proposed in the current study, can also be applied to RAFF $n$  pulses. The expected degree of  $B_0$  and  $B_1^+$  inhomogeneities greatly depends on the target application. For body imaging at 3T, commonly observed off-resonances and  $B_1^+$  inhomogeneities are in the range of  $\pm 300$  Hz, and  $\pm 60\%$ , respectively.<sup>39–42</sup> In the knee cartilage, only a limited number of studies has investigated  $B_0$  and  $B_1^+$  inhomogeneities. However, a reduced impact for both  $B_0$  ( $< 150$  Hz) and  $B_1^+$  ( $> 75\%$ ) inhomogeneities has been reported.<sup>33</sup> These applications may be sufficiently covered by the design regions chosen for the girRAFF pulses. However, for imaging at ultra-high fields, a similar optimization of higher-order RAFF pulses may provide a promising way to further improve off-resonance tolerances. Thus, the comparison of girRAFF with higher-order RAFF pulses and their combination with a parametrization approach remain interesting subjects for future work.

The bandwidth of a single pulse module was studied in the simulation and phantom experiments (Figure 2). Phantom experiments closely reproduced the results from simulations, with the exception of a lower resolution and the contribution of relaxation effects during (gir)RAFF preparations. Relaxation effects caused a minor reduction in preparation efficiency values in the optimal plateau region for phantom experiments. This effect is more visible for girRAFF, which has longer preparation time, than with RAFF. In both cases, however, the difference in preparation efficiency between simulations and phantom experiments was  $< 4\%$  in the plateau region thanks to the

use of only a single (gir)RAFF module and a phantom with long relaxation times (Spectrasyn  $T_{1\rho, \text{adiab}}/T_{2\rho, \text{adiab}} = 176.16$  ms/ $98.53$  ms<sup>17,43</sup>). Thus, the preparation efficiency variations due to relaxation effects in phantom did not overshadow those caused by field inhomogeneities targeted by the study. However, to obtain reliable quantification, multiple repetitions of the pulse module are required to enable sufficient sampling of the relaxation curve. The girRAFF module is 7.82 times longer than RAFF (Figure 1C), thus, requiring fewer repetitions to achieve the same preparation duration. Taking the in vivo relaxation time ( $T_{\text{RAFF}} = 34 \pm 1$  ms vs.  $T_{\text{girRAFF}} = 50 \pm 1$  ms), effectively 5.32 times fewer repetitions are needed for comparable relaxation curve sampling. As a result, the differences in bandwidth between girRAFF and RAFF are further exacerbated in phantom and in vivo mapping results, leading to an overall  $+504.1\%$  bandwidth increase in girRAFF versus RAFF for phantom mapping experiments, compared with 66.67% in single module phantom experiments.

This study has several limitations. The proposed pulse optimization was only applied to RAFF in the second RFR, as this pulse was available for reference comparison. Nevertheless, the approach could be applied to a wide variety of pulses for rotating frame relaxometry, such as continuous-wave and adiabatic  $T_{1\rho}$  and  $T_{2\rho}$  preparations, higher-order RAFF $n$  pulses, and more, as resilience to field inhomogeneities remains a common limiting factor at high field strengths. Furthermore, only a small number of healthy subjects were included in the evaluation of the pulses. Ultimately, thoroughly characterizing the sensitivity of novel relaxation parameters to pathological alterations in tissue composition is necessary to validate their diagnostic value. The theoretical sensitivity to molecular motion at different correlation times derived in this and previous studies<sup>20</sup> for girRAFF and RAFF pulses does not capture the true complexity of relaxation processes in vivo. The model used was limited to dipole–dipole interactions and neglected contributions from other relaxation mechanisms, such as chemical exchange and diffusion, which are important drivers of in vivo rotating-frame relaxation. Thus, ultimately only in vivo clinical validation can fully determine the parameter sensitivity and diagnostic values of the proposed  $T_{\text{girRAFF}}$  relaxation.

Finally, the proposed technique was only tested in vivo on the calf muscle and the knee cartilage, where both  $B_0$  and  $B_1^+$  inhomogeneities are limited in normal conditions. Other anatomies, like the heart or the liver, might present stronger field inhomogeneities and, thus, benefit more from the use of an optimized girRAFF preparation for rotating frame relaxation mapping. The scope of this study was kept on anatomies characterized by rather

homogeneous  $B_0$  and  $B_1^+$  fields to avoid introducing additional confounders in the quantitative analysis of the pulse performance.

## 5 | CONCLUSIONS

Our results show that SL relaxation measurements using RAFF exhibit moderate resilience against off-resonances but strong susceptibility to  $B_1^+$  inhomogeneities. A parameterized RAFF (girRAFF) formulation allowed for the derivation of preparation pulses with improved resilience against field inhomogeneities in phantom. Quantitative mapping obtained with girRAFF showed only minor variations across field inhomogeneities in vivo. Thus, girRAFF may provide a promising tool for clinical applications in body imaging at 3T where larger off-resonance resilience is needed. Further investigation of its sensitivity toward pathological remodeling is warranted.

## ACKNOWLEDGMENTS

The authors would like to thank Dr. Paul de Bruin from Philips for his support with sequence development and testing at Holland PTC. This work is supported by ERC grant (VascularID, ERC StG 101078711).

## ORCID

Chiara Coletti  <https://orcid.org/0000-0001-5994-2834>

Joao Tourais  <https://orcid.org/0000-0002-1388-4023>

Sebastian Weingärtner  <https://orcid.org/0000-0002-0739-6306>

## REFERENCES

- Weingärtner S, Desmond KL, Obuchowski NA, et al. Development, validation, qualification, and dissemination of quantitative MR methods: overview and recommendations by the ISMRM quantitative MR study group. *Magn Reson Med*. 2022;87:1184-1206.
- Binks DA, Hodgson RJ, Ries ME, et al. Quantitative parametric MRI of articular cartilage: a review of progress and open challenges. *Br J Radiol*. 2013;86:20120163.
- Banjar M, Horiuchi S, Gedeon DN, Yoshioka H. Review of quantitative knee articular cartilage MR imaging. *Magn Reson Med Sci*. 2022;21:29-40.
- Emanuel KS, Kellner LJ, Peters MJM, Haartmans MJJ, Hooijmans MT, Emans PJ. The relation between the biochemical composition of knee articular cartilage and quantitative MRI: a systematic review and meta-analysis. *Osteoarthr Cartil*. 2022;30:650-662.
- Cao G, Gao S, Xiong B. Application of quantitative T1, T2 and T2\* mapping magnetic resonance imaging in cartilage degeneration of the shoulder joint. *Sci Rep*. 2023;13:4558.
- Sepponen RE, Pohjonen JA, Sipponen JT, Tanttu JI. A method for T1p imaging. *J Comput Assist Tomogr*. 1985;9:1007-1011.
- Palmer AG, Massi F. Characterization of the dynamics of biomacromolecules using rotating-frame spin relaxation NMR spectroscopy. *Chem Rev*. 2006;106:1700-1719.
- Wang L, Chang G, Xu J, et al. T1rho MRI of menisci and cartilage in patients with osteoarthritis at 3T. *Eur J Radiol*. 2012;81:2329-2336.
- Han Y, Liimatainen T, Gorman RC, Witschey WRT. Assessing Myocardial Disease Using T1p MRI. 2014.
- Boudreau M, Keenan KE, Stikov N. Quantitative T1 and T1p mapping. *Advances in Magnetic Resonance Technology and Applications*. Vol 1. Elsevier; 2020:19-45.
- Rautiainen J, Nissi MJ, Salo EN, et al. Multiparametric MRI assessment of human articular cartilage degeneration: correlation with quantitative histology and mechanical properties. *Magn Reson Med*. 2015;74:249-259.
- Wang YJ, Zhang Q, Li X, Chen W, Ahuja A, Yuan J. T1p magnetic resonance: basic physics principles and applications in knee and intervertebral disc imaging. *Quant Imaging Med Surg*. 2015;5:858-885.
- Witschey II, Borthakur A, Elliott MA, et al. Artifacts in T1p-weighted imaging: compensation for B1 and B0 field imperfections. *J Magn Reson*. 2007;186:75-85.
- Garwood M, Delabarre L. The return of the frequency sweep: designing adiabatic pulses for contemporary NMR. *J Magn Reson*. 2001;153:155-177.
- Michaeli S, Sorce DJ, Springer CS Jr, Ugurbil K, Garwood M. T1p MRI contrast in the human brain: modulation of the longitudinal rotating frame relaxation shutter-speed during an adiabatic RF pulse. *J Magn Reson*. 2006;181:135-147.
- Mangia S, Liimatainen T, Garwood M, Michaeli S. Rotating frame relaxation during adiabatic pulses vs. conventional spin lock: simulations and experimental results at 4 T. *Magn Reson Imaging*. 2009;27:1074-1087.
- Coletti C, Fotaki A, Tourais J, et al. Robust cardiac T1 p mapping at 3T using adiabatic spin-lock preparations. *Magn Reson Med*. 2023;90(4):1363-1379.
- Sorce DJ, Michaeli S, Garwood M. Relaxation during adiabatic radiofrequency pulses. *Curr Anal Chem*. 2007;3: 239-251.
- Michaeli S, Sorce DJ, Garwood M. T2p and T1p adiabatic relaxations and contrasts. *Curr Anal Chem*. 2008;4:8-25.
- Liimatainen T, Sorce DJ, O'Connell R, Garwood M, Michaeli S. MRI contrast from relaxation along a fictitious field (RAFF). *Magn Reson Med*. 2010;64:983-994.
- Liimatainen T, Mangia S, Ling W, et al. Relaxation dispersion in MRI induced by fictitious magnetic fields. *J Magn Reson*. 2011;209:269-276.
- Yla-Herttuala E, Laidinen S, Laakso H, Liimatainen T. Quantification of myocardial infarct area based on T RAFFn relaxation time maps-comparison with cardiovascular magnetic resonance late gadolinium enhancement, T1p and T2 in vivo. *J Cardiovasc Magn Reson*. 2018;20:1-10.
- Hakkarainen H, Sierra A, Mangia S, et al. MRI relaxation in the presence of fictitious fields correlates with myelin content in normal rat brain. *Magn Reson Med*. 2016;75:161-168.
- Johnson CP, Wang L, Tóth F, et al. Quantitative MRI helps to detect hip ischemia: preclinical model of Legg-calve-Perthes disease. *Radiology*. 2018;289:386-395.
- Mirmojarabian SA, Lammentausta E, Liukkonen E, et al. Myocardium assessment by relaxation along fictitious field,

- extracellular volume, feature tracking, and myocardial strain in hypertensive patients with left ventricular hypertrophy. *Int J Biomed Imaging*. 2022;2022:1-9.
26. Tourais J, Demirel OB, Tao Q, et al. Myocardial approximate spin-lock dispersion mapping using a simultaneous  $T_{\{2\}}$  and  $T_{\{RAFF2\}}$  mapping at 3T MRI. *2022 44th Annual International Conference of the IEEE Engineering in Medicine & Biology Society (EMBC)*. IEEE; 2022:1694-1697.
  27. Tourais J, Ploem T, van Zadelhoff TA, van de Steeg-Henzen, Oei EHG, Weingärtner S. Rapid whole-knee quantification of cartilage using  $T_{\{1\}}$ ,  $T_{\{2\}}^*$ , and  $T_{\{RAFF2\}}$  mapping with magnetic resonance fingerprinting. *IEEE Trans Biomed Eng*. 2023;70(11):3197-3205.
  28. Filip P, Svatkova A, Carpenter AF, et al. Rotating frame MRI relaxations as markers of diffuse white matter abnormalities in multiple sclerosis. *NeuroImage Clin*. 2020;26:102234.
  29. Liimatainen T, Hakkarainen H, Mangia S, et al. MRI contrasts in high rank rotating frames. *Magn Reson Med*. 2015;73:254-262.
  30. Guido VR, Drake Fred L, Harris Charles R, et al. Python 3 reference manual. 2009.
  31. Akçakaya M, Basha TA, Weingärtner S, Roujol S, Berg S, Nezafat R. Improved quantitative myocardial T2 mapping: impact of the fitting model. *Magn Reson Med*. 2015;74:93-105.
  32. Captur G, Gatehouse P, Keenan KE, et al. A medical device-grade T1 and ECV phantom for global T1 mapping quality assurance—the T1 mapping and ECV standardization in cardiovascular magnetic resonance (TIMES) program. *J Cardiovasc Magn Reson*. 2016;18:58.
  33. Kim J, Peng Q, Wu C, Li X. MR  $T_{1\rho}$  preparations: B1 and B0 inhomogeneity response on 3T and 7T systems. *ISMRM and SMRT Annual Meeting and Exhibition*. ISMRM; 2021.
  34. Hänninen NE, Liimatainen T, Hanni M, Gröhn O, Nieminen MT, Nissi MJ. Relaxation anisotropy of quantitative MRI parameters in biological tissues. *Sci Rep*. 2022;12:12155.
  35. Hänninen N, Rautiainen J, Rieppo L, Saarakkala S, Nissi MJ. Orientation anisotropy of quantitative MRI relaxation parameters in ordered tissue. *Sci Rep*. 2017;7:9606.
  36. Ellermann J, Ling W, Nissi MJ, et al. MRI rotating frame relaxation measurements for articular cartilage assessment. *Magn Reson Imaging*. 2013;31:1537-1543.
  37. Rautiainen J, Nissi MJ, Liimatainen T, Herzog W, Korhonen RK, Nieminen MT. Adiabatic rotating frame relaxation of MRI reveals early cartilage degeneration in a rabbit model of anterior cruciate ligament transection. *Osteoarthr Cartil*. 2014;22:1444-1452.
  38. Wang L, Nissi MJ, Tóth F, et al. Multiparametric MRI of epiphyseal cartilage necrosis (osteochondrosis) with histological validation in a goat model. *PLoS One*. 2015;10:e0140400.
  39. Roberts NT, Hinshaw LA, Colgan TJ, Ii T, Hernando D, Reeder SB. B0 and B1 inhomogeneities in the liver at 1.5 T and 3.0 T. *Magn Reson Med*. 2021;85:2212-2220.
  40. Azlan CA, di Giovanni P, Ahearn TS, Semple SIK, Gilbert FJ, Redpath TW. B1 transmission-field inhomogeneity and enhancement ratio errors in dynamic contrast-enhanced MRI (DCE-MRI) of the breast at 3T. *J Magn Reson Imaging*. 2010;31:234-239.
  41. Weingärtner S, Zimmer F, Metzger GJ, Uğurbil K, van de Moortele PF, Akçakaya M. Motion-robust cardiac B1+ mapping at 3T using interleaved bloch-siegert shifts. *Magn Reson Med*. 2017;78:670-677.
  42. Kellman P, Hansen MS. T1-mapping in the heart: accuracy and precision. *J Cardiovasc Magn Reson*. 2014;16:1-20.
  43. Coletti C, Tourais J, van de Steeg-Henzen C, Weingärtner S. Adiabatic  $T_{2\rho}$  mapping in the human myocardium at 3T. *J Cardiovasc Magn Reson*. 2024;26:100223.
  44. Maurice G. Formal theory of spin-lattice relaxation. *J Magn Reson*. 2001;149:160-187.
  45. Oorschot Joep WM, El AH, Lorkeers SJ, et al. Endogenous assessment of chronic myocardial infarction with  $T_{1\rho}$ -mapping in patients. *J Cardiovasc Magn Reson*. 2014;16:104.
  46. Van Oorschot Joep WM, Fredy V, Eikendal Anouk LM, et al. Single breath-hold  $T_{1\rho}$ -mapping of the heart for endogenous assessment of myocardial fibrosis. *Invest Radiol*. 2016;51:505-512.
  47. Oorschot Joep WM, Fatih G, Sanne J, et al. Endogenous assessment of diffuse myocardial fibrosis in patients with  $T_{1\rho}$ -mapping. *J Magn Reson Imaging*. 2017;45:132-138.
  48. Aurelien B, Xavier P, Soumaya S, et al. Assessment of myocardial injuries in ischemic and non-ischemic cardiomyopathies using magnetic resonance T1-rho mapping. *Eur Heart J Cardiovasc Imaging*. 2023;25(4):548-557.
  49. Anup S, Damodar R, Mohammad H, et al.  $T_{1\rho}$  MRI of healthy and fibrotic human livers at 1.5 T. *J Transl Med*. 2015;13:1-7.
  50. Shuangshuang X, Qing L, Yue C, et al. Impact of liver fibrosis and fatty liver on T1rho measurements: a prospective study. *Korean J Radiol*. 2017;18:898-905.
  51. Azadeh S, Ding X, Gregory C, Regatte RR. Biexponential  $T_{1\rho}$  relaxation mapping of human knee cartilage in vivo at 3 T. *NMR Biomed*. 2017;30:e3760.
  52. Akella Sarma V, Reddy RR, Gougoutas Alexander J, et al. Proteoglycan-induced changes in  $T_{1\rho}$ -relaxation of articular cartilage at 4T. *Magn Reson Med*. 2001;46:419-423.
  53. Wheaton Andrew J, Dodge George R, Arijitt B, Bruce KJ, Ralph SH, Ravinder R. Detection of changes in articular cartilage proteoglycan by  $T_{1\rho}$  magnetic resonance imaging. *J Orthop Res*. 2005;23:102-108.
  54. Kester Benjamin S, Carpenter Philip M, Yu HJ, et al.  $T_{1\rho}/T_2$  mapping and histopathology of degenerative cartilage in advanced knee osteoarthritis. *World J Orthop*. 2017;8:350.
  55. Heckelman Lauren N, Smith Wyatt AR, Riofrio Alexie D, et al. Quantifying the biochemical state of knee cartilage in response to running using T1rho magnetic resonance imaging. *Sci Rep*. 2020;10:1870.
  56. Arijitt B, Matthew S, Christos D, Trojanowski John Q, Clark CM.  $T_{1\rho}$  MRI of Alzheimer's disease. *Neuroimage*. 2008;41:1199-1205.
  57. Mohammad H, Anup S, Kejia C, et al. T1rho ( $T_{1\rho}$ ) MR imaging in Alzheimers' disease and Parkinson's disease with and without dementia. *J Neurol*. 2011;258:380-385.
  58. Wang L, Xiaoxia W, Fujie J, et al. Adding quantitative T1rho-weighted imaging to conventional MRI improves specificity and sensitivity for differentiating malignant from benign breast lesions. *Magn Reson Imaging*. 2024;108:98-103.
  59. Umamaheswar D, Harish P, Michael F, et al. Quantitative  $T_{1\rho}$  magnetic resonance imaging of RIF-1 tumors in vivo: detection

of early response to cyclophosphamide therapy. *Cancer Res.* 2001;61:7747-7753.

60. Villanueva-Meyer JE, Barajas RF Jr, Mabray MC, et al. Differentiation of brain tumor-related edema based on 3D T1rho imaging. *Eur J Radiol.* 2017;91:88-92.
61. Ai QYH, Chen W, So TY, et al. Quantitative T1ρ MRI of the head and neck discriminates carcinoma and benign hyperplasia in the nasopharynx. *Am J Neuroradiol.* 2020;41:2339-2344.

## SUPPORTING INFORMATION

Additional supporting information may be found in the online version of the article at the publisher's website.

**Figure S1.** (A) Radiofrequency (RF) shapes: amplitude modulation, frequency modulation, and phase for the changing parametric behavior of  $\theta$  with respect to RAFF ( $\theta = 0^\circ$ ,  $\nu = 1$  and  $\rho = 1$ ) as default. (B) Corresponding magnetization behavior for all RF shapes in the first rotating frame of reference. Indicating the magnetization vector ( $M(t)$ , orange) with its trajectory and the effective field ( $B_{\text{eff}}(t)$ , blue).

**Figure S2.** (A) Radiofrequency (RF) shapes: amplitude modulation, frequency modulation, and phase for the changing parametric behavior of  $\rho$  with respect to RAFF ( $\theta = 0^\circ$ ,  $\nu = 1$  and  $\rho = 1$ ) as default. (B) Corresponding magnetization behavior for all RF shapes in the first rotating frame of reference. Indicating the magnetization vector ( $M(t)$ , orange) with its trajectory and the effective field ( $B_{\text{eff}}(t)$ , blue).

**Figure S3.** (A) Radiofrequency (RF) shapes: amplitude modulation, frequency modulation, and phase for the changing parametric behavior of  $\nu$  with respect to RAFF ( $\theta = 0^\circ$ ,  $\nu = 1$  and  $\rho = 1$ ) as default. (B) Corresponding magnetization behavior for all RF shapes in the first rotating frame of reference. Indicating the magnetization vector ( $M(t)$ , orange) with its trajectory and the effective field ( $B_{\text{eff}}(t)$ , blue).

**Figure S4.** (A) Radiofrequency (RF) shapes: amplitude modulation, frequency modulation, and phase for the changing parametric behavior of the line  $\rho = \nu\sqrt{2}$  with respect to RAFF ( $\theta = 0^\circ$ ,  $\nu = 1$  and  $\rho = 1$ ) as default. (B) Corresponding magnetization behavior for all RF shapes in the first rotating frame of reference. Indicating the magnetization vector ( $M(t)$ , orange) with its trajectory and the effective field ( $B_{\text{eff}}(t)$ , blue).

**Figure S5.**  $T_{\text{RAFF}}$  and  $T_{\text{girRAFF}}$  relaxation times obtained in various vials of the T1MES phantom as a function of the  $T_1$  (a) and  $T_2$  time (b). Linear regression analysis shows no correlation with  $T_1$  times for either  $T_{\text{RAFF}}$  and  $T_{\text{girRAFF}}$ . A linear dependence on  $T_2$  times is observed for both RAFF and girRAFF. However, differential behavior remains visible, especially for short  $T_2$  times (b, right plot).

**Figure S6.**  $T_{\text{RAFF}}$  and  $T_{\text{girRAFF}}$  relaxation times obtained in various vials of the T1MES phantom as a function of the

$T_1$  (a) and  $T_2$  time (b). Linear regression analysis shows no correlation with  $T_1$  times for either  $T_{\text{RAFF}}$  and  $T_{\text{girRAFF}}$ . A linear dependence on  $T_2$  times is observed for both RAFF and girRAFF. However, differential behavior remains visible, especially for short  $T_2$  times (b, right plot).

**Figure S7.** Second set of (A-B) phantom and (C-D) in-vivo calf RAFF and girRAFF maps obtained for each combination of  $(\Delta\omega_1^{\text{off}}, \eta_1) \in \{-150, 0, 150\} \text{ Hz} \times \{0.5, 0.75, 1.0\}$ . This set of maps was acquired with shorter RAFF preparation durations ( $T_{\text{prep,RAFF}} = 16.5, 34.0, 67.9$  ms), to account for the shorter in vivo  $T_{\text{RAFF}}$  relaxation times and achieve comparable relaxation decay sampling between RAFF and girRAFF. Trends are comparable to those observed in the first set of phantom and calf maps, displayed in Figure 5. Both phantom and calf  $T_{\text{RAFF}}$  maps show high variability across inhomogeneity combinations.  $T_{\text{girRAFF}}$  maps, on the other hand, depict improved resilience to system imperfections.

**Figure S8.** Magnetization trajectory length, computed as the cumulative sum of the discretised angular distances covered by the magnetization vector on the Bloch sphere during simulations. The trajectory length is measured in radians and low trajectory length ( $< 3.2\pi$  rad) cases were discarded to avoid idle parameter configurations yielding low power pulses with high preparation efficiency but no spin-lock relaxation.

**How to cite this article:** Coletti C, Naaktgeboren R, Tourais J, Van De Steeg-Henzen C, Weingärtner S. Generalized inhomogeneity-resilient relaxation along a fictitious field (girRAFF) for improved robustness in rotating frame relaxometry at 3T. *Magn Reson Med.* 2024;92:2373-2391. doi: 10.1002/mrm.30219

## APPENDIX.

Relaxation rates were derived for both RAFF and girRAFF methods using second-order perturbation theory of dipole-dipole interactions.<sup>20,44</sup> The relaxation rates during amplitude- and frequency-modulated RF irradiation were previously described for a system of nuclei with spin  $I$  and gyromagnetic ratio  $\gamma$  by Michaeli et al. in Eq. 7 and 8 of Reference 19, as:

$$R_{1\rho,\text{adiab}}(t) = \frac{1}{10k_{dd}} \left[ \frac{3\sin^2\alpha(t)\cos^2\alpha(t)}{1 + \omega_{\text{eff}}^2(t)\tau_c^2} + \frac{3\sin^4\alpha(t)}{1 + 4\omega_{\text{eff}}^2(t)\tau_c^2} \right. \\ \left. \frac{2 + 3\sin^2\alpha(t)}{1 + \omega_0^2\tau_c^2} + \frac{8 - 6\sin^2\alpha(t)}{1 + 4\omega_0^2\tau_c^2} \right]. \quad (\text{A1})$$

and

$$R_{2\rho,\text{adiab}}(t) = \frac{1}{40k_{dd}} \left[ 3(3\cos^2\alpha(t) - 1)^2 + \frac{30\sin^2\alpha(t)\cos^2\alpha(t)}{1 + \omega_{\text{eff}}^2(t)\tau_c^2} + \frac{3\sin^4\alpha(t)}{1 + 4\omega_{\text{eff}}^2(t)\tau_c^2} + \frac{20 - 6\sin^2\alpha(t)}{1 + \omega_0^2\tau_c^2} + \frac{8 + 12\sin^2\alpha(t)}{1 + 4\omega_0^2\tau_c^2} \right], \quad (\text{A2})$$

where

$$1/k_{dd} = 2I(I + 1)\hbar^2\gamma^2r^{-6}\tau_c. \quad (\text{A3})$$

Here,  $\hbar$  is the reduced Planck constant ( $\hbar = 1.0546 \times 10^{-34}$  Js),  $r$  is the internuclear distance ( $r = 1.58 \text{ \AA}$ ,  $\tau_c$  is the correlation time and  $\alpha(t) = \tan^{-1}\left(\frac{\omega_1(t)}{\Delta\omega(t)}\right)$ .

To compute RAFF and girRAFF relaxation rates for different correlation times  $\tau_c$ , RAFF and girRAFF amplitude and frequency-modulation functions can be used to extract the (gir)RAFF pulse amplitude  $\omega_1(t)$ , its off-resonance  $\Delta\omega(t)$  and the effective field amplitude  $\omega_{\text{eff}}(t)$ . The effective field evolution throughout the preparation pulse was obtained from Bloch simulations and used to derive the resulting  $R_{1\rho,\text{adiab}}$  and  $R_{2\rho,\text{adiab}}$  at each time point. Using a quasi-static approximation, the final relaxation during RAFF or girRAFF irradiation can then be expressed as:

$$R_{(\text{gir})\text{RAFF}} = \frac{1}{2T_p} \int_0^{T_p} (AR_{1\rho,\text{adiab}}(t) + BR_{2\rho,\text{adiab}}(t)) dt, \quad (\text{A4})$$

where  $A = \cos^2(\delta(t))$  and  $B = \sin^2(\delta(t))$ , with  $\delta(t)$  as the angle between the magnetization and the effective field.

$R_{\text{RAFF}}$  and  $R_{\text{girRAFF}}$  relaxation rates were compared with  $R_{1\rho}$ ,  $R_{2\rho}$ ,  $R_{1\rho,\text{adiab}}$  and  $R_{2\rho,\text{adiab}}$  for different correlation times. Conventional  $T_{1\rho}$  and  $T_{2\rho}$  relaxation was obtained for a constant-amplitude on-resonance RF irradiation, with  $\omega_1 = 500$  Hz and  $T_p = 30$  ms. Adiabatic spin-lock preparations were obtained using hyperbolic secant pulses, with  $\omega_1^{\text{max}} = 500$  Hz,  $T_p = 30$  ms,  $\beta = 6.9$ ,  $f_{\text{max}} = 450$  Hz, as previously used for in vivo imaging at 3T.<sup>17,43</sup>

Figure S5 shows the relaxation rates and relaxation times as a function of the correlation time  $\tau_c$ . Relaxation rates of RAFF and girRAFF fall between  $R_{1\rho,\text{adiab}}$  and  $R_{2\rho,\text{adiab}}$  and show similar trends across the range of correlation times. The relaxation time trend of RAFF and girRAFF show less similarity to conventional continuous wave  $R_{1\rho}$  and  $R_{2\rho}$  at a single frequency. Compared with  $R_{\text{RAFF}}$ ,  $R_{\text{girRAFF}}$  falls closer to  $R_{1\rho,\text{adiab}}$ . Together with the relaxation rates observed in phantom and in vivo, these results suggest that  $R_{\text{girRAFF}}$  exhibits intermediate contrast weighting between  $R_{\text{RAFF}}$  and  $R_{1\rho,\text{adiab}}$ . Thus, girRAFF may be a promising candidate for the depiction of pathologies, that have been studied with  $T_{1\rho,\text{adiab}}$  and  $T_{\text{RAFF}}$ , including myocardial and in the liver fibrosis,<sup>45-51</sup> cartilage degeneration and concentration of proteoglycans,<sup>52-55</sup> Alzheimer's and Parkinson's diseases,<sup>56,57</sup> breast tissue lesions,<sup>58</sup> and tumors.<sup>59-61</sup>